Programming nonlinear mechanical responses by topology optimization of limit-point instabilities

Zongliang Du[a,b], Tanghuai Bian[a,b], Yunhang Guo[c], Zhiang Xu[a], Anxian Huang[a], Huajian Gao[d,*] and Xu Guo[a,*]

[a]State Key Laboratory of Structural Analysis Optimization and CAE Software for Industrial Equipment, Department of Engineering Mechanics, Dalian University of Technology, Dalian, 116023, China

[b]DUT-BSU Joint Institute, Dalian University of Technology, Dalian, 116023, China

[c]Beijing Aerospace Technology Institute, Beijing, 100072, China

[d]Mechano-X Institute, Applied Mechanics Laboratory, Department of Engineering Mechanics, Tsinghua University, Beijing, 100084, China

ARTICLE INFO

Keywords:
Tailored force–displacement responses
Post-buckling behavior
Limit-point instability
Large deformation
Topology optimization
Architected structures

ABSTRACT

Limit-point instabilities provide a powerful but underexplored mechanism for programming nonlinear mechanical responses. However, integrating such instabilities into topology optimization under large deformation remains challenging due to path-tracking and geometric regularity issues. Here, we develop an explicit design framework that programs prescribed force–displacement curves by deliberately exploiting limit-point instabilities over large deformation. We extend the Moving Morphable Void (MMV) method with finite-deformation equilibrium tracing and a curvature regularization that suppresses nonphysical sharp features while retaining design freedom. The framework synthesizes architectures that realize strain-hardening-type, yield-plateau-type, and strain-softening-type structural responses under compressive strains up to 20%, with typical curve-matching errors on the order of 1–2%. Mechanistically, the macroscopic response is governed not only by instability onset but by the spatial distribution, sequential activation, and coupling of buckling and snap-through modes embedded in the topology. We demonstrate overload protection, low-frequency vibration isolation, and instability-driven energy dissipation, and extract low-dimensional parametric templates that preserve the deformation mechanisms while enabling efficient retuning. The results establish controlled limit-point instability as a systematic design resource for programming constitutive-like nonlinear behavior at the structural level.

1. Introduction

Advanced architected structures and materials with programmable mechanical responses have attracted growing interest [1, 2] due to their potential to realize tailored stiffness, stability, and energy conversion characteristics beyond those of homogeneous solids. Through geometric design, such systems can exhibit pronounced nonlinear force–displacement behavior, enabling functionalities [3–7] such as vibration isolation [8–12], impact mitigation [13, 14], and energy absorption [15–18]. From a mechanics perspective, these behaviors can be interpreted as structural-level constitutive responses arising from controlled deformation mechanisms.

Among the various strategies for generating nonlinear responses, elastic instability plays a central role [19, 20]. Buckling [21–23], snap-through [24–26], and multistability [27–30] provide access to negative stiffness, force plateaus, and large-amplitude reversible deformation. By exploiting these phenomena, a wide range of programmable mechanical systems has been developed, including stepped metamaterials [31], bistable assemblies [32, 33], and modular instability-based architectures [34, 35]. Beyond intrinsic instability, additional approaches have been proposed to tune post-buckling responses through geometric perturbations, precompression, or active control [36–38].

Despite these advances, most existing designs rely on predefined unstable elements and iterative tuning guided by designer intuition. As a result, the attainable response space is limited, and the systematic exploration of novel instability-enabled architectures remains challenging. More fundamentally, the mechanical behavior of these systems is governed by complex interactions among multiple instability modes, load-path redistributions, and large-deformation kinematics, which are difficult to control using modular or trial-and-error approaches.

gao.huajian@tsinghua.edu.cn (H. Gao); guoxu@dlut.edu.cn (X. Guo)
ORCID(s): 0000-0002-5924-438X (Z. Du)

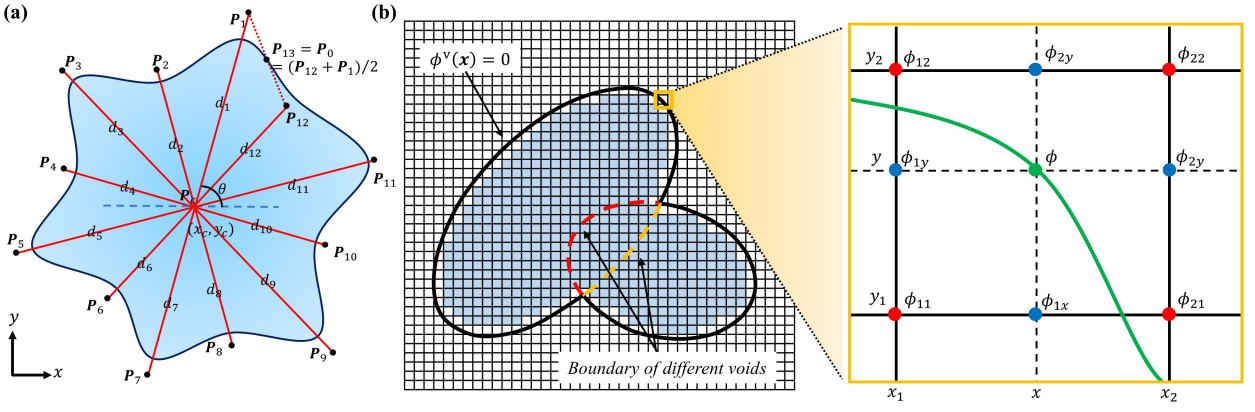

Fig. 1. (a) Schematic illustration of the Moving Morphable Void (n=12); (b) element-wise bilinear approximation of the nodal ϕ^v values.

Topology optimization provides a systematic framework for structural design and has recently been extended to nonlinear and large-deformation regimes [39, 40]. Several studies have demonstrated the possibility of programming prescribed force–displacement responses using material nonlinearity, composite layouts, or microstructural design [41–45]. However, compression-induced instabilities and post-buckling responses have received comparatively limited attention. In most topology optimization studies, buckling is treated as a failure mode to be avoided [46–49], rather than as a controllable design resource. Moreover, existing inverse-design approaches rarely address the numerical challenges associated with tracing equilibrium paths through limit-point instabilities under finite deformation, nor do they provide explicit control over geometric regularity and reusability.

These limitations raise several unresolved questions: How can limit-point instabilities be systematically incorporated into topology optimization? How can smooth and mechanically admissible topologies be generated while retaining sufficient freedom to encode complex post-buckling behavior? And how can the resulting designs be distilled into reusable templates for practical implementation?

Motivated by these challenges, this work develops an explicit topology optimization framework for programming nonlinear mechanical responses through controlled limit-point instabilities. The Moving Morphable Void method is extended by incorporating finite-deformation equilibrium tracing and a curvature regularization that suppresses spurious geometric singularities. A response-oriented optimization formulation is introduced to directly match prescribed force–displacement curves, together with an energy-based formulation for verification. Using this framework, structures exhibiting hardening-type, plateau-type, and softening-type responses are synthesized under compressive strains up to 20%, with potential applications in overload protection [50, 51], low-frequency vibration isolation [52, 53], and energy dissipation [54, 55]. The optimized topologies reveal that macroscopic behavior is governed by the spatial distribution, sequential activation, and mechanical coupling of instability modes. Furthermore, low-dimensional parametric templates are extracted from representative designs, enabling efficient tuning while preserving the underlying deformation mechanisms. More broadly, this work establishes instability-enabled topology optimization as a systematic paradigm for programming nonlinear mechanical functionality.

The remainder of this paper is organized as follows. Section 2 presents the curvature-enhanced MMV formulation. Section 3 introduces the finite-deformation analysis, optimization models, and sensitivity analysis. Section 4 reports numerical examples and validation studies. Section 5 discusses representative applications and parametric abstractions. Section 6 discusses the mechanics of instability-enabled response programming. Section 7 concludes the paper.

2. Curvature enhanced Moving Morphable Void Method

This section introduces a curvature-enhanced Moving Morphable Void (MMV) method, in which curvature regularization is incorporated to ensure geometrically smooth and mechanically admissible structural boundaries. This enhancement is particularly important for instability-driven topology optimization under large deformation, where sharp geometric features may induce artificial stress concentrations, mesh-dependent instabilities, and poor

convergence. We first briefly review the theoretical foundation of the MMV framework, followed by a detailed description of the proposed curvature control strategy and its numerical implementation.

2.1. The classic Moving Morphable Void method

In two-dimensional scenarios, the MMV approach has been extensively investigated for representing voids using B-spline curves, with their interpolative representation expressed as:

$$\boldsymbol{C}(u)=\sum_{i=0}^{n} N_{i,p}(u)\boldsymbol{P}_i \ (0\le u\le 1), \tag{1}$$

where $\boldsymbol{P}_i=\left(x_i,y_i\right)^{\top}$, $i=0,\dots,n$ are the control points; $N_{i,p}(u)$ represents the basis function B-spline for the i-th control point of the p-th order formulated as ($p=2$ in this work):

$$N_{i,p}(u)=\frac{u-u_i}{u_{i+p}-u_i}N_{i,p-1}(u)+\frac{u_{i+p+1}-u}{u_{i+p+1}-u_{i+1}}N_{i+1,p-1}(u), p\ge 1 \tag{2}$$

and

$$N_{i,0}(u)=\begin{cases}1, & u_i\le u\le u_{i+1},\\ 0, & \text{otherwise.}\end{cases} \tag{3}$$

As shown in Fig. 1(a), an MMV is characterized through a set of design variables denoted as: $\boldsymbol{D}=(x_0,y_0,r_1,\dots,r_n,\theta)^{\top}$. Here, x_0 and y_0 denote the central coordinates; r_1,…,r_n correspond to the distances from the control points to the central point $\boldsymbol{P}_c$; θ represents the angle between vector $\overrightarrow{\boldsymbol{P}_1\boldsymbol{P}_c}$ and the horizontal axis. The coordinates of the control points are expressed as:

$$\boldsymbol{P}_i=\begin{cases}\left(x_0+r_i\cos\left((i-1)\frac{2\pi}{n}+\theta\right),y_0+r_i\sin\left((i-1)\frac{2\pi}{n}+\theta\right)\right)^{\top} & i=1,...,n,\\ (\boldsymbol{P}_1+\boldsymbol{P}_n)/2, & i=0, i=n+1.\end{cases} \tag{4}$$

Under an Eulerian mesh, the region of the i-th void can be identified by its topology description function (TDF) ϕ_i^{v} expressed as:

$$\phi_i^{\mathrm{v}}=\sqrt{(x-x_{i,0})^2+(y-y_{i,0})^2}-r_i(\theta). \tag{5}$$

Therefore, the solid and void regions are distinguished by the TDF via:

$$\begin{cases}\phi_i^{\mathrm{v}}(\boldsymbol{D};\boldsymbol{x})<0, & \text{if } \boldsymbol{x}\in\Omega_i^{\mathrm{v}}\\ \phi_i^{\mathrm{v}}(\boldsymbol{D};\boldsymbol{x})=0, & \text{if } \boldsymbol{x}\in\partial\Omega_i^{\mathrm{v}}\\ \phi_i^{\mathrm{v}}(\boldsymbol{D};\boldsymbol{x})>0, & \text{if } \boldsymbol{x}\in\Omega\backslash\left(\Omega_i^{\mathrm{v}}\cup\partial\Omega_i^{\mathrm{v}}\right)\end{cases} \tag{6}$$

Here, Ω is the design domain, Ω_i^{v} denotes the region occupied by the i-th void, $\partial\Omega_i^{\mathrm{v}}$ denotes its boundary, and $\boldsymbol{x}$ represents the spatial coordinates. To identify the overall solid region and ensure the differentiability, the global TDF of the optimized structure is expressed via the aggregation function as follows:

$$\phi^{\mathrm{v}}(\boldsymbol{x})=\min\left(\phi_1^{\mathrm{v}}(\boldsymbol{x}),\cdots,\phi_i^{\mathrm{v}}(\boldsymbol{x}),\cdots,\phi_{nv}^{\mathrm{v}}(\boldsymbol{x})\right)\approx\ln\left(\sum_{i=1}^{nv}\exp\left(\zeta\phi_i^{\mathrm{v}}(\boldsymbol{x})\right)\right)/\zeta, \tag{7}$$

where nv denotes the number of MMVs and a relatively small negative even number ζ was selected, such as $\zeta=-80$. Then the structural region can be identified by $\phi^{\mathrm{v}}(\boldsymbol{x})$ similarly according to Eq. (6). Through optimizing the design variable vector $\boldsymbol{D}$, the MMVs move and deform, resulting in an optimal structural configuration.

2.2. Curvature-enhanced strategy for improving the smoothness of structural boundaries

Optimized designs obtained using the original MMV method often contain sharp corners and geometric singularities at void intersections, as illustrated in Fig. 1(b). Under large deformation, such features may lead to artificial stress concentrations, numerical instabilities, and mesh-dependent responses. To address these issues, a curvature constraint

is introduced to suppress excessive geometric irregularities and directly generate smooth structural boundaries during optimization. The curvature along the material interface is evaluated from the TDF. On a fixed Eulerian grid, the TDF and its spatial derivatives within each grid cell are reconstructed using bilinear interpolation of nodal values, following common practice in level-set-based approaches [56]. This interpolation effectively regularizes the structural boundary by averaging over neighboring nodes, assigning sharp corners with finite curvatures and thereby facilitating stable and consistent sensitivity evaluations.

As shown in Fig. 1(b), a representative grid cell intersected by the $\phi^{\mathrm{v}} = 0$ interface is considered to illustrate the curvature interpolation procedure. The interface is discretized into a set of points, at which the curvature is evaluated pointwise and subsequently integrated along the interface. Let ϕ_{11}, ϕ_{12}, ϕ_{21}, and ϕ_{22} denote the TDF values at the four corner nodes of a grid unit with dimensions $\mathrm{d}x$ and $\mathrm{d}y$, corresponding to the grid spacings in the x- and y-directions, respectively. Introducing local coordinates $s, t \in [0, 1]$ such that $x = x_0 + s\mathrm{d}x$ and $y = y_0 + t\mathrm{d}y$, the interpolated TDF field is expressed as:

$$\phi^{\mathrm{v}}(s,t) = (1-s)(1-t)\phi_{11} + s(1-t)\phi_{21} + (1-s)t\phi_{12} + st\phi_{22}. \tag{8}$$

The spatial derivatives of the bilinearly interpolated TDF can be computed analytically, and its components are given by

$$\phi^{\mathrm{v}}_{,x} = \frac{1}{\mathrm{d}x}\left[(1-t)(\phi_{21}-\phi_{11}) + t(\phi_{22}-\phi_{12})\right], \quad \phi^{\mathrm{v}}_{,y} = \frac{1}{\mathrm{d}y}\left[(1-s)(\phi_{12}-\phi_{11}) + s(\phi_{22}-\phi_{21})\right]. \tag{9}$$

Besides, the unmixed second-order derivatives vanish (i.e., $\phi^{\mathrm{v}}_{,xx} = \phi^{\mathrm{v}}_{,yy} = 0$), while the mixed partial derivative $\phi^{\mathrm{v}}_{,xy}$ is given by

$$\phi^{\mathrm{v}}_{,xy} = \frac{1}{\mathrm{d}x\,\mathrm{d}y}(\phi_{11} - \phi_{12} - \phi_{21} + \phi_{22}). \tag{10}$$

Substituting these expressions into the curvature definition $\kappa = \nabla \cdot (\nabla\phi^{\mathrm{v}}/|\nabla\phi^{\mathrm{v}}|)$ yields

$$\kappa = \frac{-2\phi^{\mathrm{v}}_{,xy}\phi^{\mathrm{v}}_{,x}\phi^{\mathrm{v}}_{,y}}{\left((\phi^{\mathrm{v}}_{,x})^2 + (\phi^{\mathrm{v}}_{,y})^2\right)^{3/2}}. \tag{11}$$

When the $\phi^{\mathrm{v}} = 0$ interface intersects the boundary of the design domain, some interface points may fall within the outermost grid cells. In such cases, a one-sided interpolation strategy is adopted, whereby the nearest interior grid cell is used to evaluate the TDF derivatives, ensuring numerical robustness of the curvature computation.

To penalize regions of excessive curvature, a curvature constraint is introduced, defined as the arc-length integral of the squared curvature along the structural boundary:

$$E_{\mathrm{curv}} = \int_{{}^0\Gamma} |\kappa(x,y)|^2 \,\mathrm{d}^0\Gamma \le E^*_{\mathrm{curv}}, \tag{12}$$

where ${}^0\Gamma$ denotes the material interface. The upper bound E^*_{curv} is specified relative to a reference value, taken as the total curvature of circular voids in the initial design. To accommodate the increased geometric complexity arising during topology optimization, this bound is set to twice the reference value. This curvature functional acts as a geometric regularizer that penalizes excessive bending of structural boundaries. Unlike surface-energy regularization, the present formulation is introduced primarily to ensure geometric smoothness and mechanical admissibility, while preserving the essential instability mechanisms required for nonlinear response programming.

The proposed curvature-enhanced MMV formulation provides a robust geometric representation that enables stable topology optimization involving large deformation and limit-point instabilities. This geometric regularization is particularly critical for instability-enabled topology optimization, where small geometric irregularities may significantly influence post-buckling deformation paths.

3. Explicit topology optimization of post-buckled structures for tailored nonlinear responses

This section establishes the finite deformation analysis framework employed in this study, with a focus on structural responses involving limit-point instability. Within this framework, the associated topology optimization formulations

are developed. Section 3.1 details the numerical treatment of compression-induced instability under finite deformation and introduces the adopted hyperelastic constitutive model. Then Section 3.2 formulates two closely related optimization problems within an explicit topology optimization framework: a general formulation targeting prescribed force-displacement responses and a specialized maximum-energy formulation used for verification purposes. Finally, Section 3.3 derives the corresponding sensitivity expressions for the subsequent numerical implementation.

3.1. Finite deformation analysis of compressive instability

In structural analysis, bifurcation instability and limit-point instability represent fundamentally different classes of nonlinear behavior. Bifurcation-induced buckling typically requires eigenvalue analysis to identify critical modes, generally followed by the introduction of geometric imperfections to steer the numerical solver toward a specific post-buckling path [57]. This procedure is more computationally demanding and highly sensitive to imperfection choices, often resulting in strong path-dependence and non-uniqueness of the computed responses [58]. Differently, limit-point instability (or fold bifurcation) can be captured more naturally within a nonlinear equilibrium analysis. As the load increases, the structure undergoes stiffness softening, reaches a limit point, and subsequently evolves along the post-buckling equilibrium path without the need for externally imposed imperfections. This characteristic makes limit-point instability particularly attractive for the systematic exploitation of post-buckling responses in topology optimization. This property enables instability-enabled response programming without introducing artificial imperfections, thereby improving robustness and reproducibility in topology optimization.

To describe material behavior under finite deformation, the Arruda–Boyce hyperelastic constitutive model [59] is adopted to capture large-deformation hyperelastic behavior while isolating geometric nonlinearity and instability effects. The strain energy density function W is given by:

$$\begin{aligned} W = \mu \Bigg[& \frac{1}{2}(\bar{I}_1 - 3) + \frac{1}{20\lambda_m^2}(\bar{I}_1^2 - 9) + \frac{11}{1050\lambda_m^2}(\bar{I}_1^3 - 27) \\ & + \frac{19}{7000\lambda_m^2}(\bar{I}_1^4 - 81) + \frac{519}{673750\lambda_m^2}(\bar{I}_1^5 - 243) \Bigg] + \frac{1}{D_k}\left(\frac{J^2-1}{2} - \ln J\right), \end{aligned} \tag{13}$$

where μ is the initial shear modulus, λ_m denotes the network locking stretch that characterizes the maximum extensibility of polymer chains, and D_k is the incompressibility parameter. The Jacobian J represents the ratio of the deformed volume to the undeformed volume, and $\bar{I}_1$ is the first invariant of the modified right Cauchy-Green deformation tensor.

The finite deformation problem is formulated within the Total Lagrangian (TL) framework [60], in which all quantities are referred to the initial configuration. The superscript ${}^0(\cdot)$ denotes variables in the reference configuration, and ${}^0\Omega$ represents the undeformed design domain. The equilibrium of the discretized system at the i-th sampling point can be written as:

$$\boldsymbol{R}_i(\boldsymbol{U}, \boldsymbol{D}) = \boldsymbol{f}_i^{\text{int}}(\boldsymbol{U}, \boldsymbol{D}) - \boldsymbol{f}_i^{\text{ext}} = \sum_{e=1}^{ne} \boldsymbol{L}_e^\top \boldsymbol{f}_{i,e}^{\text{int}}(\boldsymbol{U}_e) - \sum_{e=1}^{ne} \boldsymbol{L}_e^\top \boldsymbol{f}_{i,e}^{\text{ext}} = \boldsymbol{0}, \tag{14}$$

where $\boldsymbol{R}_i(\boldsymbol{U}, \boldsymbol{D})$ is the residual force vector between the internal force vector $\boldsymbol{f}_i^{\text{int}}$ and the external force vector $\boldsymbol{f}_i^{\text{ext}}$. $\boldsymbol{U}$ and $\boldsymbol{U}_e$ are the global nodal displacement vector and the corresponding displacement vector of the e-th element, respectively. ne is the total number of elements in the structure, $\boldsymbol{L}_e^\top$ is the connecting matrix of the e-th element. The elemental external and internal force vectors are given by:

$$\boldsymbol{f}_{i,e}^{\text{ext}} = \int_{{}^0\Omega_e} \boldsymbol{N}^\top \boldsymbol{f}\, \mathrm{d}^0V + \int_{{}^0S_e} \boldsymbol{N}^\top \boldsymbol{t}\, \mathrm{d}^0S, \quad \boldsymbol{f}_{i,e}^{\text{int}} = \int_{{}^0\Omega_e} \boldsymbol{B}^\top(\boldsymbol{U}_e)\boldsymbol{S}\, \mathrm{d}^0V, \tag{15}$$

where $\boldsymbol{N}$ is the shape function matrix and $\boldsymbol{B}(\boldsymbol{U}_e)$ is the strain-displacement matrix under large deformation. $\boldsymbol{S}$ denotes the second Piola–Kirchhoff stress tensor derived from the constitutive relation $\boldsymbol{S} = \partial W/\partial \boldsymbol{E}$, where $\boldsymbol{E}$ denotes the Green–Lagrange strain tensor. $\boldsymbol{f}$ and $\boldsymbol{t}$ represent the body force density and surface traction, respectively, while ${}^0\Omega_e$ and ${}^0S_e$ denote the elemental domain and its boundary in the reference configuration.

For subsequent derivations, the global residual vector is decomposed into contributions associated with displacement-controlled nodes (subscript dn) and free nodes (subscript fn), yielding:

$$\boldsymbol{R}_i(\boldsymbol{U}, \boldsymbol{D}) = \left(\boldsymbol{R}_{i,\text{dn}}(\boldsymbol{U}, \boldsymbol{D}); \boldsymbol{R}_{i,\text{fn}}(\boldsymbol{U}, \boldsymbol{D})\right) = \left(\boldsymbol{f}_{i,\text{dn}}^{\text{int}}(\boldsymbol{U}, \boldsymbol{D}) - \boldsymbol{f}_{i,\text{dn}}^{\text{ext}}; \boldsymbol{f}_{i,\text{fn}}^{\text{int}}(\boldsymbol{U}, \boldsymbol{D}) - \boldsymbol{0}\right). \tag{16}$$

For problems where the structural response is monotonically increasing, the nonlinear equilibrium Eq. (14) is solved using a conventional Newton–Raphson scheme combined with displacement control. In cases involving non-monotonic responses (e.g., snap-through or snap-back behavior), the analysis is switched to an arc-length method to trace the complete equilibrium path reliably [60, 61]. As these solution techniques are well-documented in standard textbooks, their detailed description is omitted here for brevity. In finite element analyses involving large deformations, low-density (or low-stiffness) elements may result in ill-conditioned tangent stiffness matrices, severe mesh distortion, and convergence failure [62]. To alleviate numerical instabilities induced by such elements during topology optimization, the redundant degree-of-freedom removal technique [63, 64] is employed, and DOFs only related to low-density elements are eliminated. This treatment reduces the size of the global stiffness matrix and significantly improves computational efficiency.

3.2. Mathematical formulation of topology optimization design

Building on the numerical analysis framework established above, this subsection formulates the topology optimization problem within the proposed curvature-enhanced MMV paradigm. Two closely related optimization models are considered: a **response-based design** for tailoring prescribed nonlinear force-displacement behaviors, and an **energy-based design** that corresponds to a maximum strain-energy formulation. The latter can be regarded as a particular case of the former and is primarily employed for numerical validation.

3.2.1. Optimization Problem I: Post-buckled structures with tailored nonlinear responses

To systematically program nonlinear force–displacement responses, we formulate a response-oriented topology optimization problem. The objective is defined as the discrepancy between the target and realized force–displacement responses under prescribed displacement loading. Using the curvature-enhanced MMV method, the topology optimization problem in continuous form is stated as:

$$
\begin{aligned}
&\text{Find } \boldsymbol{D} = \left((\boldsymbol{D}^1)^\top, \cdots, (\boldsymbol{D}^i)^\top, \cdots, (\boldsymbol{D}^{nv})^\top\right)^\top, \quad \boldsymbol{u}(\boldsymbol{D};\boldsymbol{x}) \in \mathcal{H}^1({}^0\Omega) \\
&\text{Minimize: } \mathcal{J}_1(\boldsymbol{U}_{\mathrm{fn}}(\boldsymbol{D}), \boldsymbol{D}; \boldsymbol{U}_{\mathrm{dn}}) = \sum_{i=1}^{M} \left(\frac{F_{i,\mathrm{dn}}(\boldsymbol{U}_{i,\mathrm{fn}}, \boldsymbol{D}) - F_i^*}{\overline{F_i}^*} \right)^2 \\
&\text{S.t. } \int_{{}^0\Omega} H\left(\phi^{\mathrm{v}}(\boldsymbol{D};\boldsymbol{x})\right) \boldsymbol{S} : \delta\boldsymbol{E}\, \mathrm{d}^0\mathrm{V} = \int_{{}^0\Omega} H\left(\phi^{\mathrm{v}}(\boldsymbol{D};\boldsymbol{x})\right) \boldsymbol{f} \cdot \delta\boldsymbol{v}\, \mathrm{d}^0\mathrm{V} + \int_{{}^0S_t} \boldsymbol{t} \cdot \delta\boldsymbol{v}\, \mathrm{d}^0\mathrm{S}, \quad \forall \boldsymbol{v} \in \mathcal{U}_{\mathrm{ad}}^0 \\
&V = \int_{{}^0\Omega} H\left(\phi^{\mathrm{v}}(\boldsymbol{D};\boldsymbol{x})\right) \mathrm{d}^0\mathrm{V} \le \overline{V}, \quad \boldsymbol{u} = \overline{\boldsymbol{u}}, \text{ on } {}^0S_u, \quad \boldsymbol{D} \subset {}^0\mathcal{U}_{\boldsymbol{D}} \\
&E_{\mathrm{curv}} = \int_{{}^0\Gamma} |\kappa(x,y)|^2\, \mathrm{d}^0\Gamma \le E_{\mathrm{curv}}^*
\end{aligned}
\tag{17}
$$

This formulation directly programs the structural response rather than optimizing conventional performance metrics such as stiffness or compliance, thereby enabling inverse design of nonlinear mechanical behavior. Here, M denotes the number of sampling points along the prescribed displacement path, and $\boldsymbol{u}$ represents the displacement field defined over the design domain. $\mathcal{H}^1({}^0\Omega)$ is the first-order Sobolev space. $\boldsymbol{U}_{\mathrm{dn}}$ and $\boldsymbol{U}_{\mathrm{fn}}$ correspond to the displacement vectors at the prescribed-displacement nodes and free nodes, respectively. $\overline{F_i}^*$ denotes the mean value of the target force response F_i^*. At equilibrium, the total reaction force $F_{i,\mathrm{dn}}(\boldsymbol{U}_{i,\mathrm{fn}}, \boldsymbol{D})$ is given by the sum of the internal forces at the displacement-controlled nodes. Where ${}^0S_t$ denotes the traction boundary, $\delta\boldsymbol{v}$ is the virtual displacement, and $\mathcal{U}_{\mathrm{ad}}^0$ is the corresponding admissible space of virtual displacement. The prescribed displacement on the Dirichlet boundary ${}^0S_u$ is denoted by $\overline{\boldsymbol{u}}$. In implementation, the Heaviside function $H(x)$ is regularized as:

$$
H_\epsilon^\gamma(x) = \begin{cases} 1 & x > \epsilon \\ \frac{3(1-\gamma)}{4}\left(\frac{x}{\epsilon} - \frac{x^3}{3\epsilon^3}\right) + \frac{1+\gamma}{2} & -\epsilon \le x \le \epsilon \\ \gamma & \text{otherwise} \end{cases}
\tag{18}
$$

where ϵ controls the width of the transition zone and γ is a small positive parameter. In the present study, $\epsilon = 0.1$ and $\gamma = 10^{-6}$ are adopted at the initial stage of optimization.

Under finite element discretization, the volume fraction is evaluated as:

$$V = \sum_{e=1}^{ne} \frac{V_e}{V_D} \left(\frac{1}{nn} \sum_{j=1}^{nn} H_\epsilon^\gamma (\phi^{\mathrm{v}})_j^e \right), \tag{19}$$

where nn is the number of nodes per element. V_e and V_D denote the volume of the e-th element and the design domain, respectively.

3.2.2. Optimization Problem II: Structures for maximum stored energy

For numerical verifications, a second optimization problem is considered, aiming to maximize the total stored strain energy, equivalently, the area enclosed by the force-displacement curve over a prescribed displacement interval. This formulation differs from Optimization Problem I only in the objective function, while all constraints and modeling assumptions remain unchanged as Eq. (17). It serves as a verification case and illustrates the generality of the proposed framework.

Let h denote the uniform displacement increment. The corresponding objective function is defined as:

$$\mathcal{J}_2(\boldsymbol{U}_{\mathrm{fn}}(\boldsymbol{D}), \boldsymbol{D}; \boldsymbol{U}_{\mathrm{dn}}) = -\sum_{i=1}^{M} \left(\frac{h}{2} (F_{i-1,\mathrm{dn}}(\boldsymbol{U}_{\mathrm{fn}}, \boldsymbol{D}) + F_{i,\mathrm{dn}}(\boldsymbol{U}_{\mathrm{fn}}, \boldsymbol{D})) \right) \tag{20}$$

Together, these two formulations establish a unified optimization framework that spans from general nonlinear response tailoring to energy-based structural design. The sensitivity analysis for both problems is presented in the following subsection.

3.3. Sensitivity Analysis

3.3.1. Sensitivity analysis of post-buckled structures with tailored nonlinear responses

Sensitivity analysis is essential for efficient topology optimization, particularly for instability-driven problems involving multiple equilibrium states. The sensitivities of the objective function in Problem I with respect to the design variables are derived using an adjoint-based approach. Without loss of generality, body forces are neglected in the following derivations. An augmented Lagrangian functional is constructed as:

$$L_1(\boldsymbol{U}, \boldsymbol{D}) = \mathcal{J}_1(\boldsymbol{U}_{\mathrm{fn}}(\boldsymbol{D}), \boldsymbol{D}; \boldsymbol{U}_{\mathrm{dn}}) + \sum_{i=1}^{M} \boldsymbol{\lambda}_i^\top \boldsymbol{R}_i(\boldsymbol{U}, \boldsymbol{D}), \tag{21}$$

where $\boldsymbol{\lambda}_i$ denotes the adjoint displacement vector corresponding to the i-th sampling point. Taking the total derivative of L_1 with respect to the design variables yields:

$$\frac{\partial L_1(\boldsymbol{U}, \boldsymbol{D})}{\partial \boldsymbol{D}} = \sum_{i=1}^{M} \left(\boldsymbol{\lambda}_{i,\mathrm{dn}}^\top \frac{\partial \boldsymbol{f}_{i,\mathrm{dn}}^{\mathrm{int}}}{\partial \boldsymbol{D}} + \boldsymbol{\lambda}_{i,\mathrm{fn}}^\top \frac{\partial \boldsymbol{f}_{i,\mathrm{fn}}^{\mathrm{int}}}{\partial \boldsymbol{D}} \right). \tag{22}$$

The adjoint variables associated with the displacement-controlled nodes and the free nodes are obtained from the stationarity conditions as:

$$\boldsymbol{\lambda}_{i,\mathrm{dn}}^\top = 2 \frac{F_{i,\mathrm{dn}} - F_i^*}{\left(\overline{F}_i^*\right)^2} \mathbf{I}, \qquad \boldsymbol{\lambda}_{i,\mathrm{fn}}^\top = -2 \frac{F_{i,\mathrm{dn}} - F_i^*}{\left(\overline{F}_i^*\right)^2} \frac{\partial \boldsymbol{f}_{i,\mathrm{dn}}^{\mathrm{int}}}{\partial \boldsymbol{U}_{i,\mathrm{fn}}} \left(\frac{\partial \boldsymbol{f}_{i,\mathrm{fn}}^{\mathrm{int}}}{\partial \boldsymbol{U}_{i,\mathrm{fn}}} \right)^{-1}, \tag{23}$$

where $\mathbf{I}$ denotes the identity matrix. The derivative of the volume constraint with respect to the design variables is given by:

$$\frac{\partial V}{\partial \boldsymbol{D}} = \sum_{e=1}^{ne} \frac{V_e}{V_D} \left(\frac{1}{nn} \sum_{j=1}^{nn} \frac{\partial H_\epsilon^\gamma (\phi^{\mathrm{v}})_j^e}{\partial \phi^{\mathrm{v}}} \right) \frac{\partial \phi^{\mathrm{v}}}{\partial \boldsymbol{D}}. \tag{24}$$

Similarly, the sensitivity of the curvature constraint is obtained via the chain rule as:

$$\frac{\partial E_{\mathrm{curv}}}{\partial \boldsymbol{D}} = \int_\Gamma 2\kappa \frac{\partial \kappa}{\partial \phi^{\mathrm{v}}} \frac{\partial \phi^{\mathrm{v}}}{\partial \boldsymbol{D}} \mathrm{d}\Gamma. \tag{25}$$

The derivative of the global TDF ϕ^{v} with respect to the design variables can be expressed as:

$$\frac{\partial \phi^{\mathrm{v}}}{\partial \boldsymbol{D}} = \sum_{i=1}^{nv} \frac{\partial \phi^{\mathrm{v}}}{\partial \phi^{i}(\boldsymbol{D}^{i};\boldsymbol{x})} \frac{\partial \phi^{i}(\boldsymbol{D}^{i};\boldsymbol{x})}{\partial \boldsymbol{D}} = \sum_{i=1}^{nv} \frac{e^{\zeta \phi^{i}(\boldsymbol{D}^{i};\boldsymbol{x})}}{\sum_{j=1}^{nv} e^{\zeta \phi^{j}(\boldsymbol{D}^{j};\boldsymbol{x})}} \frac{\partial \phi^{i}(\boldsymbol{D}^{i};\boldsymbol{x})}{\partial \boldsymbol{D}}. \tag{26}$$

In Eq. (26), the explicit expressions for $\partial \phi^{i}(\boldsymbol{D}^{i};\boldsymbol{x})/\partial \boldsymbol{D}$ are provided in Appendix A. The derivative of the curvature κ with respect to the global TDF ϕ^{v} reads:

$$\begin{aligned}\frac{\partial \kappa}{\partial \phi^{\mathrm{v}}} =& -\frac{\partial}{\partial x}\left[2\phi^{\mathrm{v}}_{,xy}\phi^{\mathrm{v}}_{,y}((\phi^{\mathrm{v}}_{,x})^2+(\phi^{\mathrm{v}}_{,y})^2)^{-5/2}((\phi^{\mathrm{v}}_{,y})^2-2(\phi^{\mathrm{v}}_{,x})^2)\right]-\frac{\partial}{\partial y}\left[2\phi^{\mathrm{v}}_{,xy}\phi^{\mathrm{v}}_{,x}((\phi^{\mathrm{v}}_{,x})^2+(\phi^{\mathrm{v}}_{,y})^2)^{-5/2}(2(\phi^{\mathrm{v}}_{,y})^2-(\phi^{\mathrm{v}}_{,x})^2)\right]\\ &+\frac{\partial^2}{\partial x\partial y}\left[-2\phi^{\mathrm{v}}_{,x}\phi^{\mathrm{v}}_{,y}((\phi^{\mathrm{v}}_{,x})^2+(\phi^{\mathrm{v}}_{,y})^2)^{-3/2}\right].\end{aligned} \tag{27}$$

3.3.2. Sensitivity analysis of structures for maximum stored energy

Similarly, to solve the problem in Section 3.2.2, this section derives the corresponding sensitivities. An augmented Lagrangian functional is constructed by introducing adjoint displacement vectors $\boldsymbol{\lambda}_i$ associated with each sampling point along the loading path, while explicitly accounting for the residual contribution from the preceding sample point:

$$L_2(\boldsymbol{U},\boldsymbol{D}) = \mathcal{J}_2(\boldsymbol{U}_{\mathrm{fn}}(\boldsymbol{D}),\boldsymbol{D};\boldsymbol{U}_{\mathrm{dn}}) + \sum_{i=1}^{M}\left(\boldsymbol{\lambda}_i^{\top}\boldsymbol{R}_i(\boldsymbol{U},\boldsymbol{D}) + \boldsymbol{\lambda}_{i-1}^{\top}\boldsymbol{R}_{i-1}(\boldsymbol{U},\boldsymbol{D})\right), \tag{28}$$

where $\boldsymbol{\lambda}_i$ denotes the adjoint displacement vector corresponding to the i-th sample point. The sensitivity of $L_2(\boldsymbol{U},\boldsymbol{D})$ with respect to the design variables is then computed as:

$$\frac{\partial L_2(\boldsymbol{U},\boldsymbol{D})}{\partial \boldsymbol{D}} = \sum_{i=1}^{M}\left(\boldsymbol{\lambda}_{i,\mathrm{dn}}^{\top}\frac{\partial \boldsymbol{f}^{\mathrm{int}}_{i,\mathrm{dn}}}{\partial \boldsymbol{D}} + \boldsymbol{\lambda}_{i,\mathrm{fn}}^{\top}\frac{\partial \boldsymbol{f}^{\mathrm{int}}_{i,\mathrm{fn}}}{\partial \boldsymbol{D}} + \boldsymbol{\lambda}_{i-1,\mathrm{dn}}^{\top}\frac{\partial \boldsymbol{f}^{\mathrm{int}}_{i-1,\mathrm{dn}}}{\partial \boldsymbol{D}} + \boldsymbol{\lambda}_{i-1,\mathrm{fn}}^{\top}\frac{\partial \boldsymbol{f}^{\mathrm{int}}_{i-1,\mathrm{fn}}}{\partial \boldsymbol{D}}\right). \tag{29}$$

From the stationarity conditions, the adjoint variables are obtained as

$$\boldsymbol{\lambda}_{i,\mathrm{dn}}^{\top} = \boldsymbol{\lambda}_{i-1,\mathrm{dn}}^{\top} = -\frac{h}{2}\mathbf{I}, \qquad \boldsymbol{\lambda}_{i-1,\mathrm{fn}}^{\top} = \frac{h}{2}\frac{\partial \boldsymbol{f}^{\mathrm{int}}_{i-1,\mathrm{dn}}}{\partial \boldsymbol{U}_{i-1,\mathrm{fn}}}\left(\frac{\partial \boldsymbol{f}^{\mathrm{int}}_{i-1,\mathrm{fn}}}{\partial \boldsymbol{U}_{i-1,\mathrm{fn}}}\right)^{-1}, \qquad \boldsymbol{\lambda}_{i,\mathrm{fn}}^{\top} = \frac{h}{2}\frac{\partial \boldsymbol{f}^{\mathrm{int}}_{i,\mathrm{dn}}}{\partial \boldsymbol{U}_{i,\mathrm{fn}}}\left(\frac{\partial \boldsymbol{f}^{\mathrm{int}}_{i,\mathrm{fn}}}{\partial \boldsymbol{U}_{i,\mathrm{fn}}}\right)^{-1}. \tag{30}$$

These expressions reveal that the adjoint operator at each sampling point is intrinsically coupled to the displacement-loading history through the preceding equilibrium state, reflecting the path-dependent nature of the limit-point instability problem. For numerical implementation, a uniform step size h is adopted throughout this work. The resulting framework enables systematic exploration of instability-enabled nonlinear responses, as demonstrated in the following numerical examples.

4. Numerical examples

This section demonstrates the capability of the proposed framework to program nonlinear mechanical responses through controlled instability. We first validate the sensitivity formulation and optimization framework. We then compare energy-based and stiffness-based formulations to illustrate the role of instability in shaping nonlinear responses. Finally, we demonstrate the inverse design of tailored nonlinear force–displacement responses. The optimization problems are solved using the Method of Moving Asymptotes (MMA) [65]. The material parameters are $\mu = 1.08\,\mathrm{MPa}$, $\lambda_m = 7$, and $D_k = 0.01$ (corresponding to a bulk modulus of 0.2 GPa). The displacement loading path is discretized into $M = 10$ sampling points. In addition, the volume constraint is applied in the initial iterations, then during the optimization process, the curvature constraint is applied. Unless otherwise stated, all numerical examples presented in the following adopt these settings.

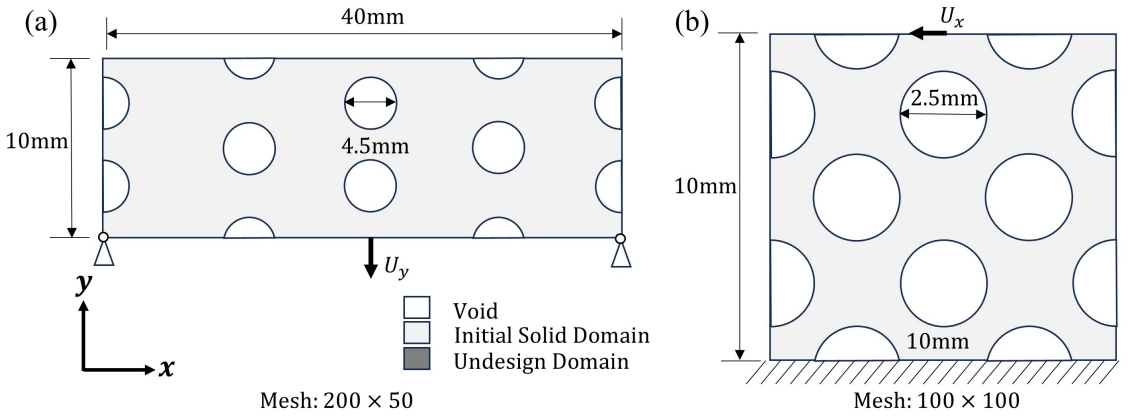

Fig. 2. Boundary conditions and initial designs for energy-based topology optimization with a constant out-of-plane thickness of 1 mm under a plane stress assumption. (a) Case 1: design domain of 40 mm × 10 mm, discretized using 200 × 50 uniform four-node bilinear quadrilateral finite elements; a prescribed downward displacement applied at the midpoint of the bottom edge. (b) Case 2: design domain of 10 mm × 10 mm, discretized using 100 × 100 uniform four-node bilinear quadrilateral finite elements; a prescribed horizontal displacement applied at the center of the top edge.

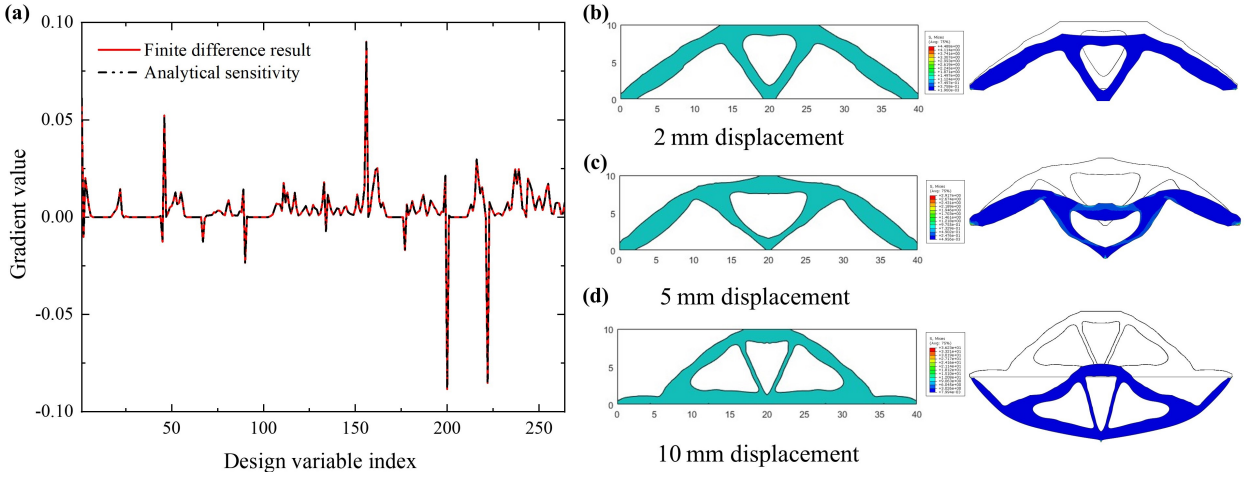

Fig. 3. (a) Differential sensitivity verification for energy-based design (Case 1); optimized designs obtained from energy-based design under maximum prescribed displacements of (b) 2 mm, (c) 5 mm, and (d) 10 mm.

4.1. Analytical sensitivity verification

This subsection validates the correctness and robustness of the proposed sensitivity formulation. We begin by examining the consistency of the derived adjoint sensitivities through finite-difference verification for the energy-based formulations presented in Sections 3.3.2, for the initial in Fig. 2. As shown in Fig. 3(a), the analytical and finite-difference sensitivities exhibit excellent agreement, confirming the correctness of the sensitivity derivations and their numerical implementation.

Based on the established formulation, a simply supported beam benchmark (**energy-based design, Case 1**) is considered to illustrate the characteristics of the proposed optimization framework. The design domain, initial MMV layout, mesh discretization, and boundary conditions are detailed in Fig. 2(a). Three maximum prescribed vertical displacements, $U_y = 2$, 5 and 10 mm, are considered in separate optimizations. The maximum volume fraction is set to 0.3 and the upper bound of the curvature constraint is set to 45.

As the prescribed displacement increases, the optimized structures shown in Fig. 3 exhibit pronounced topological variation. At $U_y = 2$ mm, the optimized structure closely resembles the result reported in [66] and deforms

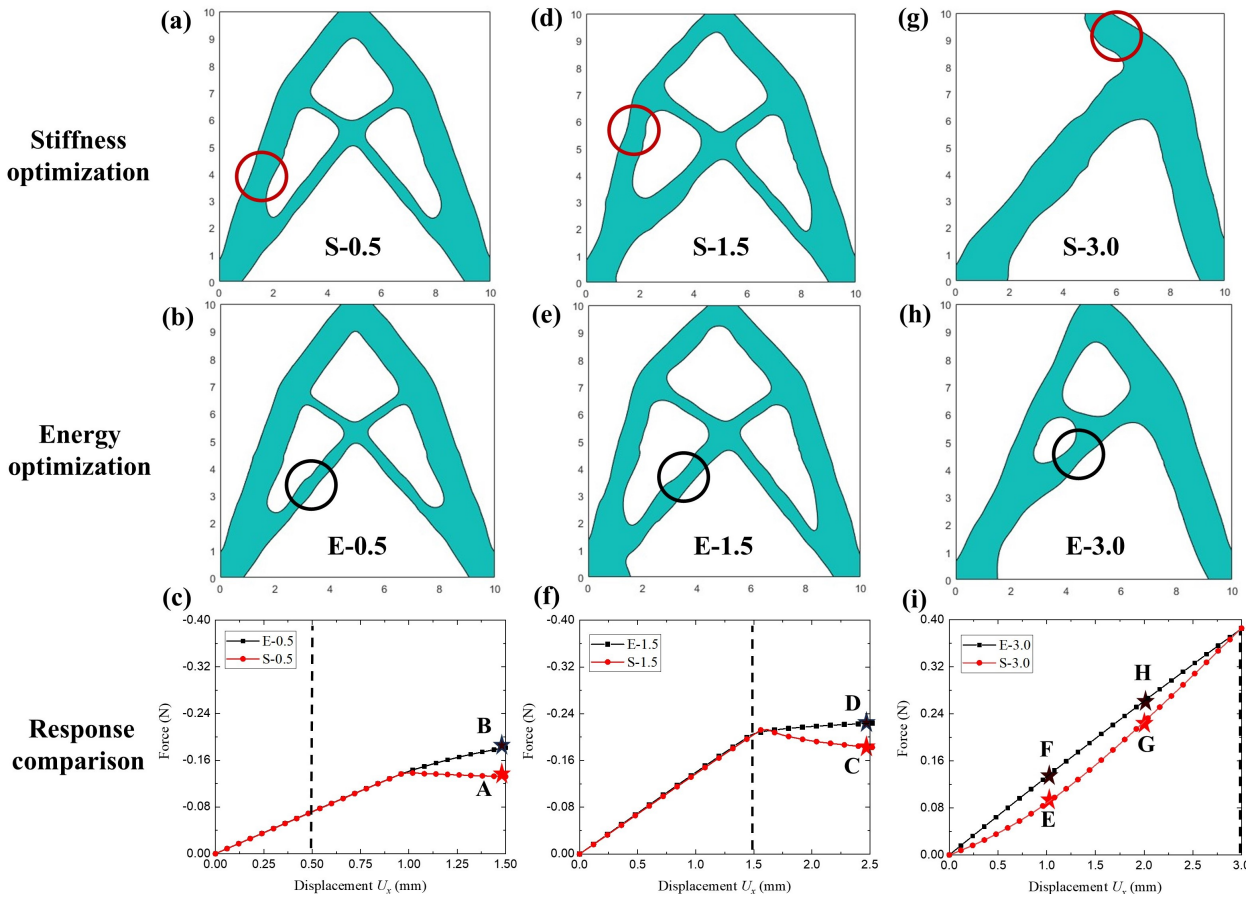

Fig. 4. Comparison of optimization results between the classic stiffness optimization (S) and the energy-based design (E) under maximum prescribed displacements of U_x=0.5, 1.5 and 3.0 mm for Case 2, respectively. Here, S-x and E-x denote the stiffness-based and energy-based designs with a prescribed maximum displacement of $U_x = x$ mm. (a), (d), (g) illustrate the designs of stiffness optimization; (b), (e), (h) illustrate the designs of energy optimization; (c), (f), (i) illustrate the force-displacement curves of the designs of stiffness optimization and energy optimization, respectively.

predominantly through bending of members connecting the central region to the supports, indicating a bending-dominated response.

When the prescribed displacement increases to 5 mm, the global topology remains similar; however, the connecting members become shorter and thicker, leading to increased bending stiffness and a growing contribution from axial compression and tension. At $U_y = 10$ mm, a clear change in optimized topology is observed: the connecting members align nearly horizontally, and the deformation becomes primarily stretching-dominated. Similar transitions from bending- to stretching-dominated mechanisms under large deformation have been reported in previous studies [66].

These results confirm the correctness of the sensitivity formulation and establish the numerical robustness of the proposed instability-enabled topology optimization framework.

4.2. Comparison of classic stiffness and energy-based optimization under prescribed displacements

To highlight the fundamental differences between the proposed energy-based formulation and conventional design strategies, classic stiffness design minimizing the end compliance is adopted as a reference. This is equivalent to maximizing structural stiffness at the prescribed displacement. The corresponding formulation is summarized in Appendix B.

The configuration shown in Fig. 2(b) is considered as the initial design, where a horizontal displacement is prescribed at the top boundary. Three maximum prescribed displacements, U_x=0.5, 1.5, and 3.0 mm, corresponding

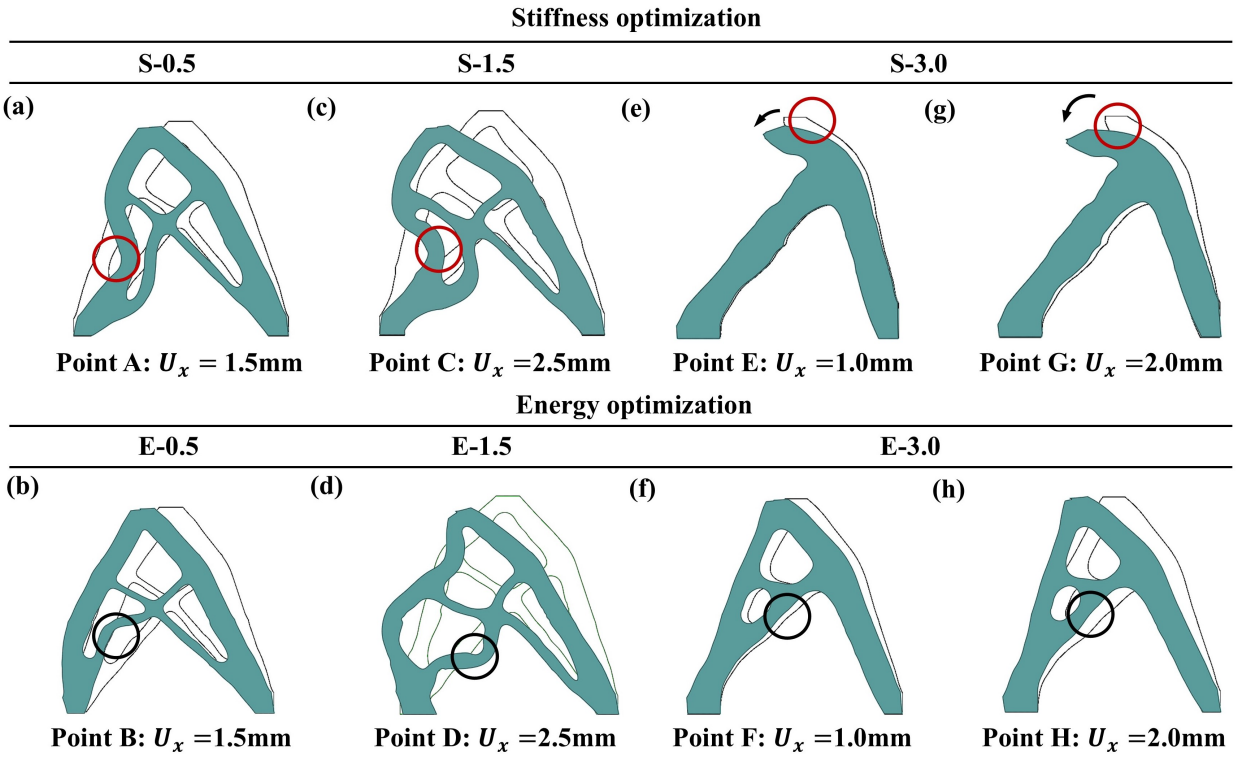

Fig. 5. Comparison of deformation configurations between the classic stiffness optimization (S) and the energy-based design (E) at representative displacement states for Case 2. The deformation states correspond to the labeled points in Fig. 4. (a–b) S-0.5 and E-0.5 at U_x = 1.5 mm; (c–d) S-1.5 and E-1.5 at U_x = 2.5 mm; (e–f) S-3.0 and E-3.0 at U_x = 1.0 mm; (g–h) S-3.0 and E-3.0 at U_x = 2.0 mm.

to nominal strains of 5%, 15%, and 30%, respectively, are examined. The maximum volume fraction is set to 0.4, and the upper bound of the curvature constraint is set to 80.

Fig. 4 shows the optimized topologies together with the corresponding force–displacement curves. Obviously, the structures optimized under prescribed maximum displacements of 0.5 and 1.5 mm are relatively similar, consisting of an outer contour "Λ" of thicker members and an inner network "x" of thinner members (Figs. 4(a–b) and (d–e)). The outer members predominantly resist the deformation, while the inner members act as secondary load-transfer paths. When the applied displacement exceeds 3 mm, both the configurations of the stiffness-based and energy-based designs vary significantly (i.e., S-3.0 and E-3.0, Fig. 4(g-i)). Specifically, S-3.0 illustrates a "λ"-shaped structure, while E-3.0 resembles a "A"-shaped structure. Their force–displacement curves also differ: E-3.0 remains approximately linear, while S-3.0 behaves as a convex force–displacement curve.

To illustrate the underlying mechanism, Fig. 5 presents representative deformed configurations at selected states. In the stiffness-based design (S-0.5), the outer member circled in red is thinner than that in the corresponding energy-based design. When the applied displacement exceeds 1.0 mm, localized buckling occurs in these weakened members, directly affecting the primary load-transfer path and reducing load-carrying capacity. In the energy-based design (E-0.5, Fig. 4(b)), the outer contour members have a more uniform thickness, and buckling occurs within the inner network (black circle), a secondary load-transfer path whose influence on the global response is less pronounced. Figs. 5(a–b) show the post-buckled deformation of S-0.5 and E-0.5 at U_x = 1.5 mm.

For the optimized designs S-1.5 and E-1.5, besides a similar mechanism, some differences remain. In S-1.5, localized thinning along the outer contour (red circle in Fig. 4(d)) leads to a larger force drop under further loading. In E-1.5, more material is distributed in the inner network while the outer components are thinner as compared to E-0.5. All these structural features lead to the post-buckled deformation at U_x = 2.5 mm shown as Figs. 5(c–d).

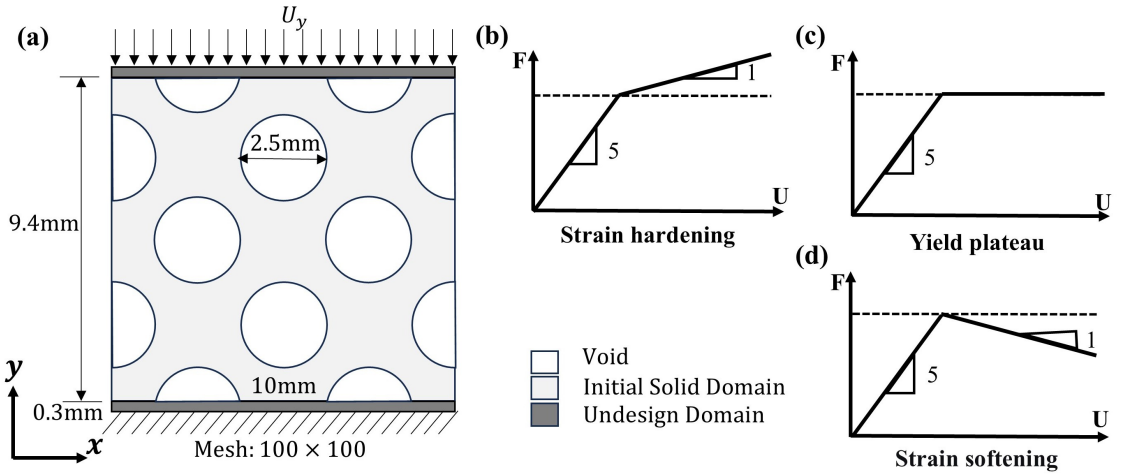

Fig. 6. (a) Boundary conditions and initial design for topology optimization of tailored nonlinear force–displacement responses with a constant out-of-plane thickness of 1 mm under a plane stress assumption. The 10 mm × 10 mm design domain is discretized using 100 × 100 uniform four-node bilinear quadrilateral finite elements. A uniform downward displacement is prescribed on the top edge, and the non-design region is shaded in gray. (b–c) Schematic illustrations of nonlinear force–displacement responses under compressive loading up to a nominal strain of 20%, with the buckling point occurring at a strain of 8%.

In the stiffness-based design S-3.0, at $U_x = 1.0$ mm (Fig. 5(e)), the response is mainly the rotation of its top (red circle), leading to a relatively small force response along the prescribed displacement. At $U_x = 2.0$ mm (Fig. 5(g)), the rotation has almost completed and the lower members begin to deform noticeably. This results in an increase in tangent stiffness in the force–displacement curve in Fig. 4(i). Differently, the energy-based design (E-3.0) shows a more uniform deformation pattern. At both $U_x = 1.0$ mm (Fig. 5(f)) and $U_x = 2.0$ mm (Fig. 5(h)), the deformation is distributed throughout the structure without pronounced localized rotations. As a result, the force–displacement curve remains nearly linear.

The observations above indicate that different optimization formulations can lead to distinct stiffness-evolution characteristics along the loading path. While conventional stiffness optimization evaluates structural performance only at the terminal displacement, the energy-based formulation implicitly regulates the structural response throughout the prescribed deformation range. On the one hand, buckling is alleviated in both the stiffness-based and energy-based design formulations to enhance the load capacity; on the other hand, appropriate post-buckling behavior supplies a novel strategy to realize various force-displacement responses as shown in the subsequent part.

These results demonstrate that instability-enabled topology optimization provides a broader design space for programming nonlinear responses compared to conventional stiffness-driven design.

4.3. Topology optimization of post-buckled structures with tailored nonlinear responses

This subsection demonstrates the inverse design of nonlinear force–displacement responses through controlled limit-point instabilities. The design domain, loading condition, and boundary constraints are illustrated in Fig. 6(a). To ensure stable load transfer and avoid numerical artifacts near the boundaries, non-designable regions of size 10 mm × 0.3 mm are introduced along the top and bottom edges.

Three representative compressive response types under large deformation, strain-hardening, yield-plateau, and strain-softening, are considered, representing distinct classes of nonlinear structural behavior governed by different instability mechanisms, as schematically shown in Figs. 6(b-d). It is emphasized that these terms describe the "overall structural force-displacement characteristics" rather than the constitutive behavior of the base material. Specifically, the target responses are characterized by a change in tangent stiffness from an initial value of 5 to post-buckling values of 1, 0, and −1, respectively. The maximum volume fraction is set to 0.4, and the upper bound of the curvature constraint is prescribed as 100.

Finite-difference verification has also been performed for Problem I, with the consistency provided in Appendix C. The optimized topologies corresponding to the three target responses are presented in Fig. 7, clearly revealing the

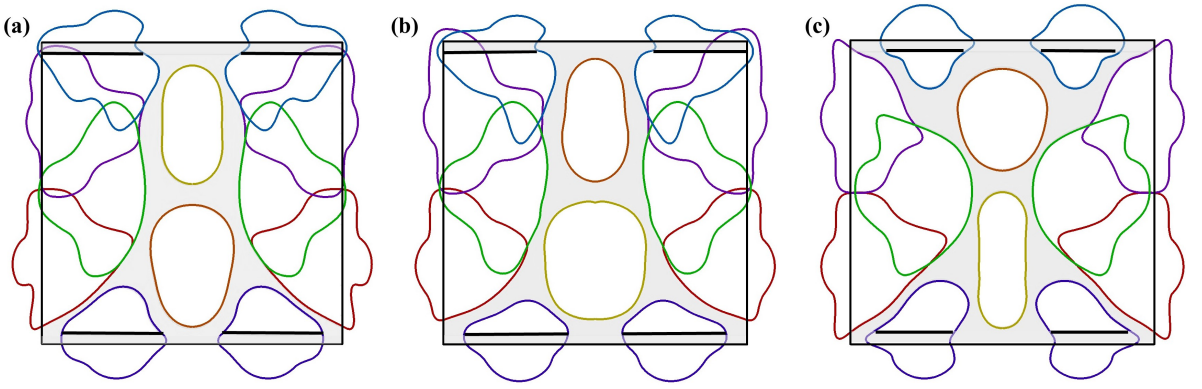

Fig. 7. Optimized structures for three prescribed nonlinear force–displacement responses: (a) strain hardening response (Design 1); (b) yield plateau response (Design 2); (c) strain softening response (Design 3).

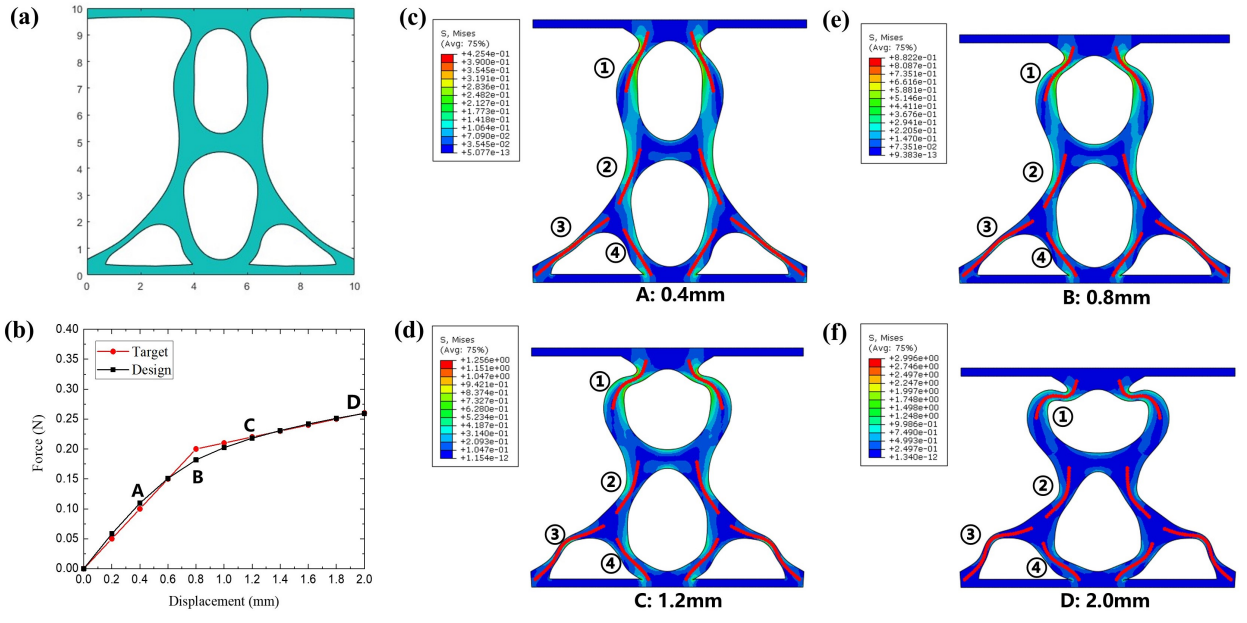

Fig. 8. Optimized design and mechanical response corresponding to a prescribed strain-hardening response. (a) Design 1. (b) Comparison between the target and obtained force–displacement curves, with four selected displacement points A (0.4 mm), B (0.8 mm), C (1.2 mm), and D (2.0 mm). (c–f) von Mises stress distributions corresponding to points A–D shown in the deformed configuration, respectively.

spatial arrangement of MMVs. Each optimized structure is further analyzed in terms of its geometric configuration, dominant deformation mechanism, and resulting force-displacement response. In addition, the three optimized designs can be interpreted as modular building blocks that may serve as primitive units for subsequent structural assembly. By arranging these modules in series or in parallel, more complex and programmable mechanical responses can be constructed, highlighting the extensibility of the proposed design framework.

4.3.1. Post-buckled structures with strain hardening response

Using the framework presented above, we first design a structural module exhibiting a strain-hardening response with a prescribed reduction in stiffness. As shown in Fig. 8, Design 1 targets a bilinear force–displacement curve in which the stiffness decreases from 0.25 N/mm to 0.05 N/mm. The optimized result achieves a relative error of 1.5%, indicating excellent agreement with the target response. The optimized structure consists of an "8"-shaped primary load-bearing frame supplemented by two inclined auxiliary rods.

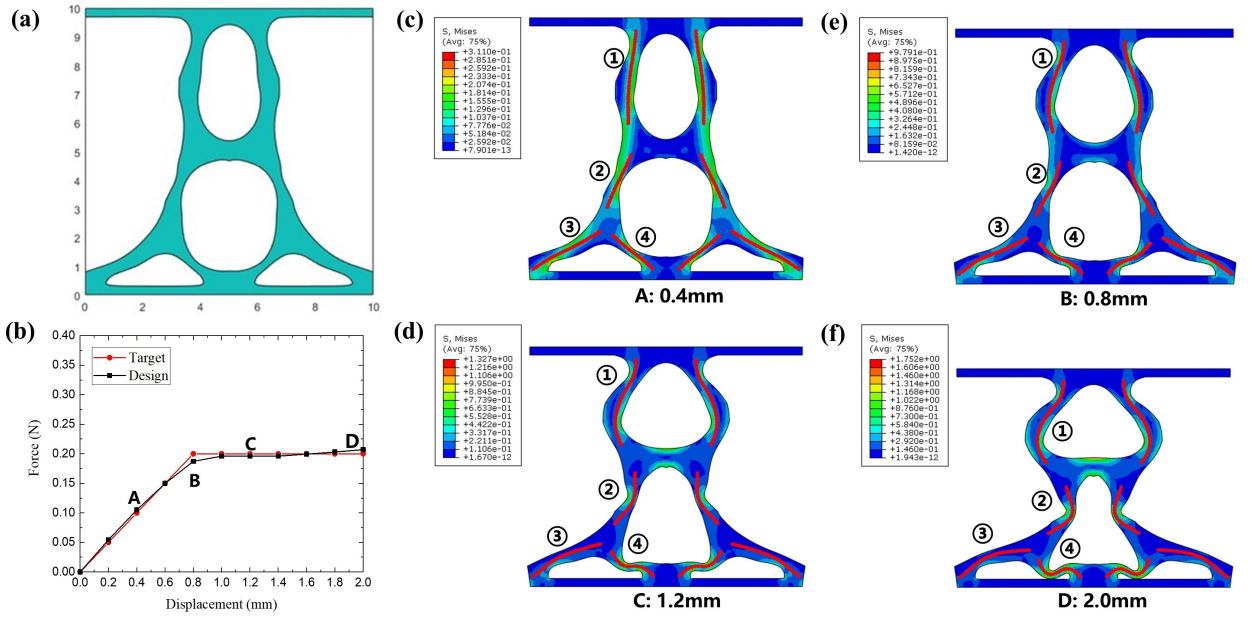

Fig. 9. Optimized design and mechanical response corresponding to a prescribed yield plateau response. (a) Design 2. (b) Comparison between the target and obtained force–displacement curves, with four selected displacement points A (0.4 mm), B (0.8 mm), C (1.2 mm), and D (2.0 mm). (c–f) von Mises stress distributions corresponding to points A–D shown in the deformed configuration, respectively.

The strain-hardening behavior originates from a transition from axial-dominated load transfer to bending-dominated deformation within the primary structural frame. The representative deformation states shown in Figs. 8(c–f) illustrate this progressive evolution with highlighted regions. At a small displacement (0.4 mm, point A in the force-displacement curve in Fig. 8(b)), load is efficiently transmitted through axial compression along the primary load path, resulting in a relatively high initial stiffness. As deformation progresses, bending gradually becomes dominant in the curved segments of the primary frame (region ①), while regions ② and ④ exhibit much smaller curvature and continue to deform primarily through axial compression. This evolution weakens the axial force transmission and continuously reduces the tangent stiffness, with a limit-point instability occurring in the inclined auxiliary members (region ③) that modulate stiffness without altering the global deformation mode.

In summary, Design 1 exemplifies how the interplay between primary-frame bending and auxiliary-member instabilities can be exploited to achieve a smooth, strain-hardening response. This case highlights the principle of regulating post-buckling behavior through structural topology, which sets the stage for the following examples exploring yield-plateau and strain-softening responses. This example illustrates how localized instability can be used to gradually modulate stiffness.

4.3.2. Post-buckled structures with yield plateau response

Force-displacement responses featuring a force plateau are of particular interest due to their potential applications. Using the proposed optimization framework, as shown in Fig. 9(b), Design 2 first exhibits a stiffness of 0.25 N/mm and transitions to a nearly constant-force regime at a displacement of approximately 0.8 mm. The optimized response achieves a relative error of 1.08%, confirming accurate realization of the prescribed plateau behavior.

As illustrated in Fig. 9(c–f), the yield plateau emerges from the coordinated response of multiple limit-point instabilities. At a downward displacement of 0.8 mm, regions ① and ④ are buckled, while regions ② and ③ show milder deformation, consistent with the actual weakened response in Fig. 9(b). As the displacement progresses to 1.2 mm, the post-buckling bending in region ② becomes more pronounced, followed closely by region ③. These distributed instabilities collectively effect the load capacity, maintaining a nearly constant global force over a finite displacement interval.

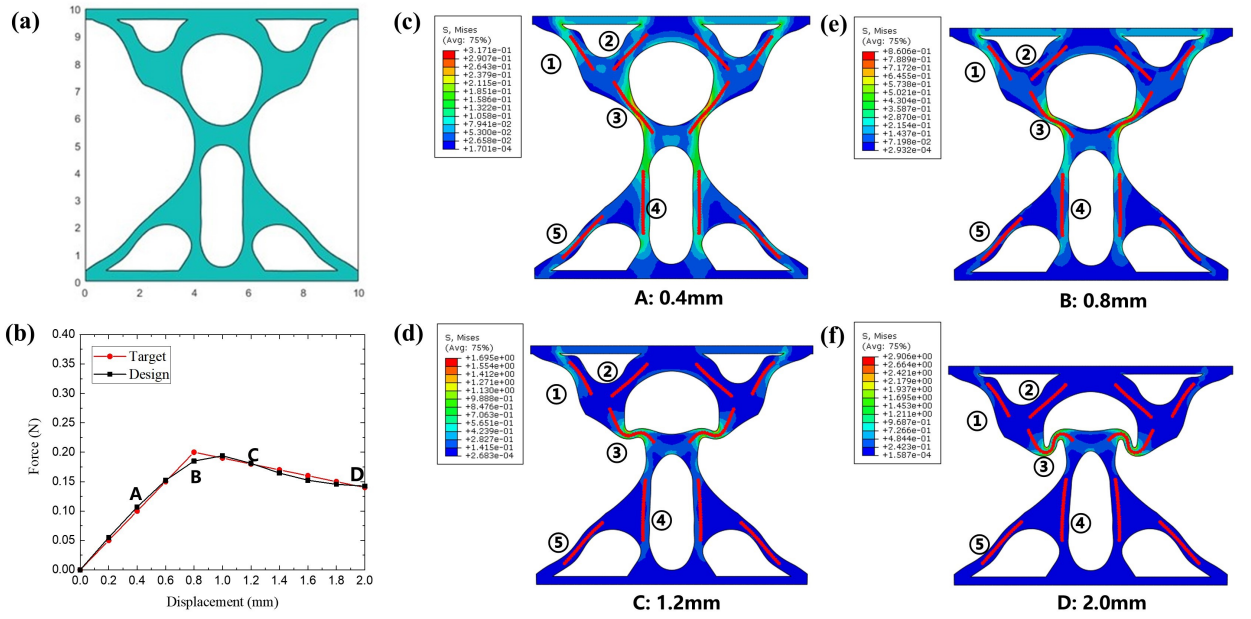

Fig. 10. Optimized design and mechanical response corresponding to a prescribed strain softening response. (a) Design 3. (b) Comparison between the target and obtained force–displacement curves, with four selected displacement points A (0.4 mm), B (0.8 mm), C (1.2 mm), and D (2.0 mm). (c–f) von Mises stress distributions corresponding to points A–D shown in the deformed configuration, respectively.

This mechanism differs fundamentally from many quasi-zero-stiffness systems in literature, which typically combine a discrete negative-stiffness element with an independent positive-stiffness spring arranged in parallel [67, 68]. Differently, the present continuum configuration contains no separable stiffness components, and the instability is distributed throughout the structure.

In short, Design 2 realizes a nearly constant-force plateau through the coordinated limit-point instabilities of multiple structural components. This example highlights how structural configuration can distribute and regulate post-buckling behavior to achieve a stable, extended plateau response. This case demonstrates how distributed instabilities generate plateau-type responses.

4.3.3. Post-buckled structures with strain softening response

We next design a structure exhibiting a strain softening (negative stiffness) response induced by a controlled snap-through instability. In Design 3, the target force-displacement response consists of an initial positive stiffness of 0.25 N/mm, followed by a transition to a negative stiffness regime with a slope of −0.05 N/mm beyond a prescribed displacement of $d = 0.8$ mm. The optimized topology achieves a relative error of 1.9% in force-displacement response.

As shown in Fig. 10, the optimized design differs markedly from the previous cases and consists of two central voids interconnected by non-uniform oblique members. The obtained force–displacement curve in Fig. 10(b) captures the intended snap-through behavior, with the limit point of the force-displacement curve located at approximately 1.0 mm, slightly shifted from the target value.

Deformed configurations in Figs. 10(c–f) illustrate the progressive localization of the stress field under instability. At a downward displacement of 0.4 mm, a relatively uniform stress distribution along regions ①–⑤ as the load transmission path, resulting in a relatively stiff response. As deformation increases, higher-level stress gradually concentrates toward the central structural segment. Consequently, a snap-through instability appeared in region ③, producing the negative tangent stiffness observed in Fig. 10(b). This strain softening behavior arises purely from geometrically induced instability and remains fully reversible, in contrast to material softening.

In conclusion, the nonlinear response of Design 3 is generated through a localized snap-through instability to trigger branch switching. This contrasts with the stiffness degradation of Design 1 and the distributed instability cascade of Design 2, highlighting the ability of the proposed framework to toggle between fundamentally different instability

architectures in order to achieve prescribed nonlinear mechanical responses. This example highlights snap-through instability as a mechanism for negative stiffness.

4.3.4. Summary

The three examples demonstrate distinct topological architectures for prescribing nonlinear force–displacement responses through geometrically induced instability. Design 1 produces a strain-hardening response through a transition from axial-dominated load transfer to bending-dominated deformation, with a local limit-point instability in the two inclined auxiliary rods subtly modulating the overall stiffness. Design 2 achieves a yield-plateau response via the coordinated activation of distributed local limit points. This distributed mechanism maintains an approximately constant global force-displacement response over a finite displacement interval. Design 3 generates a strain-softening response through a concentrated snap-through instability accompanied by branch switching, producing a negative stiffness segment. Taken together, these cases illustrate how structural topology can regulate not only the magnitude of stiffness but also the spatial distribution and coordination of instability events, enabling systematic transitions between continuous deformation, distributed criticality, and concentrated snap-through mechanisms.

Appendix D presents additional optimized structures exhibiting various combinations of initial stiffness and post-instability responses, including transitions from 0.25 N/mm to 0.1 N/mm, from 0.1 N/mm to 0.05 N/mm, from 0.2 N/mm to zero stiffness, and from 0.25 N/mm to negative stiffness (-1 N/mm). These supplementary examples further demonstrate the versatility and generality of the proposed topology optimization framework for tailoring nonlinear force-displacement behaviors.

These examples demonstrate that nonlinear mechanical responses can be systematically programmed by controlling the spatial distribution and activation sequence of limit-point instabilities. The programmable nonlinear responses provide a foundation for practical applications, as demonstrated in the following section.

5. Applications of optimized structures with tailored nonlinear responses

This section illustrates how instability-programmed nonlinear responses can be leveraged for representative mechanical functionalities, including overload protection, vibration isolation, and energy dissipation. These examples are intended to demonstrate the mechanical implications of the proposed design framework rather than to provide fully optimized engineering designs.

5.1. Overload protection via strain hardening response

Most existing overload-protection designs are based on idealized elastic-plastic models, in which an initial elastic regime is followed by a plastic stage with reduced tangent stiffness. In such systems, overload protection is typically achieved through irreversible plastic deformation, which dissipates energy and, owing to the reduced post-yield stiffness, confines the final deformation within a predictable range [51, 69]. The present study targets an analogous protective mechanism, but realized purely through geometric nonlinearity. Since a hyperelastic material model is adopted, energy dissipation through plasticity is not available. Instead, the reduced stiffness in the post-buckling regime serves to limit the deformation of the protected component, provide a clear mechanical indication of overload, and ensure a controlled and predictable response.

A snap-through structure is selected as the protected component, as illustrated in Fig. 11(a). Without protection, the component rapidly loses stability and undergoes snap-through under loading, leading to severe stress concentration (Fig. 11(b)). The component is made of silicon, with an elastic modulus of 170 GPa and a Poisson's ratio of 0.22. A prescribed displacement of 2 mm is applied in both the unprotected and protected configurations.

In the protected system, the strain-hardening structure (Design 1) is connected in series with the protected component, as shown in Fig. 11(d). Owing to this series configuration, the global force-displacement response is governed by the softer element after the stiffness transition. As a result, the reaction force remains relatively low (black curve in Fig. 11(c)), while the protected component experiences only negligible deformation (Fig. 11(e)), effectively bounding its final displacement within a small range (Fig. 11(f)). These results demonstrate that the strain-hardening post-buckling structure can function as a passive mechanical fuse, providing effective overload protection without relying on irreversible material damage. This example highlights how instability-enabled stiffness transitions can be used to regulate load transfer and protect sensitive components.

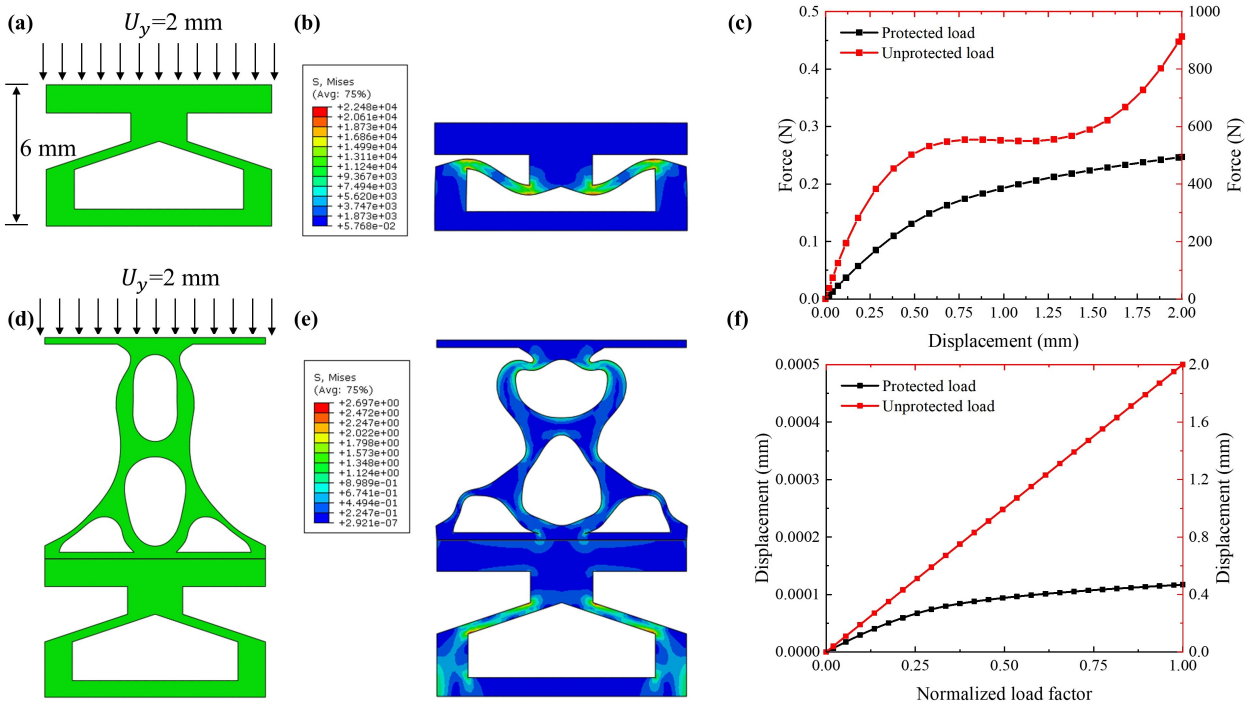

Fig. 11. Illustration of a strain hardening structure for overload protection: (a) unprotected component and loading configuration; (b) von Mises stress distribution of the unprotected component after loading; (c) comparison of force-displacement curves for the protected and unprotected components; (d) protected system with Design 1 connected in series and its loading configuration; (e) von Mises stress distribution of the protected component after loading; (f) comparison of displacement responses for the protected and unprotected components along the displacement loading.

5.2. Vibration isolation via yield plateau response

Building on the yield plateau responses designed in Section 4.3.2, this section demonstrates how the combination of a post-buckling-induced force plateau and a subsequent positive-stiffness regime can be exploited for vibration isolation. Such yield-plateau structures can exhibit QZS-like behavior, simultaneously providing sufficient static stiffness to support static loads and low effective dynamic stiffness under small-amplitude excitations.

Most existing QZS isolators rely on multi-component assemblies, such as spring-actuated linkages or cam-roller mechanisms [70, 71], which inevitably increase structural complexity and assembly sensitivity. In contrast, the present framework realizes the plateau response using a single-phase continuum structure obtained via topology optimization, offering a compact and mechanically integrated solution for low-frequency vibration isolation.

As shown in Fig. 12(b), contact constraints are enforced to ensure physically admissible deformations under large strains. The nominal strain considered in the optimization problem is 20%, and actually the force plateau extends from 8% to 58% nominal strain, followed by a rapid increase in load-bearing capacity caused by contact. This behavior confirms that the optimized structure exhibits a stable QZS-like response over a broad displacement range, consistent with practical requirements for vibration isolation.

To evaluate the vibration isolation performance, a mass block was placed on the designed structure to preload it into the QZS regime. Harmonic displacement excitation was then applied at the bottom surface under different damping ratios η, and the resulting displacement response at the top surface of the mass was recorded to compute the displacement transmissibility T_u [72], defined as

$$T_u = 20\log_{10}\left(\frac{A_{\text{out}}}{A_{\text{in}}}\right), \tag{31}$$

where A_{in} and A_{out} denote the input and output displacement amplitudes, respectively. The frequency-dependent transmissibility was evaluated to assess the influence of damping on the dynamic response (Fig. 12(c)). In the absence

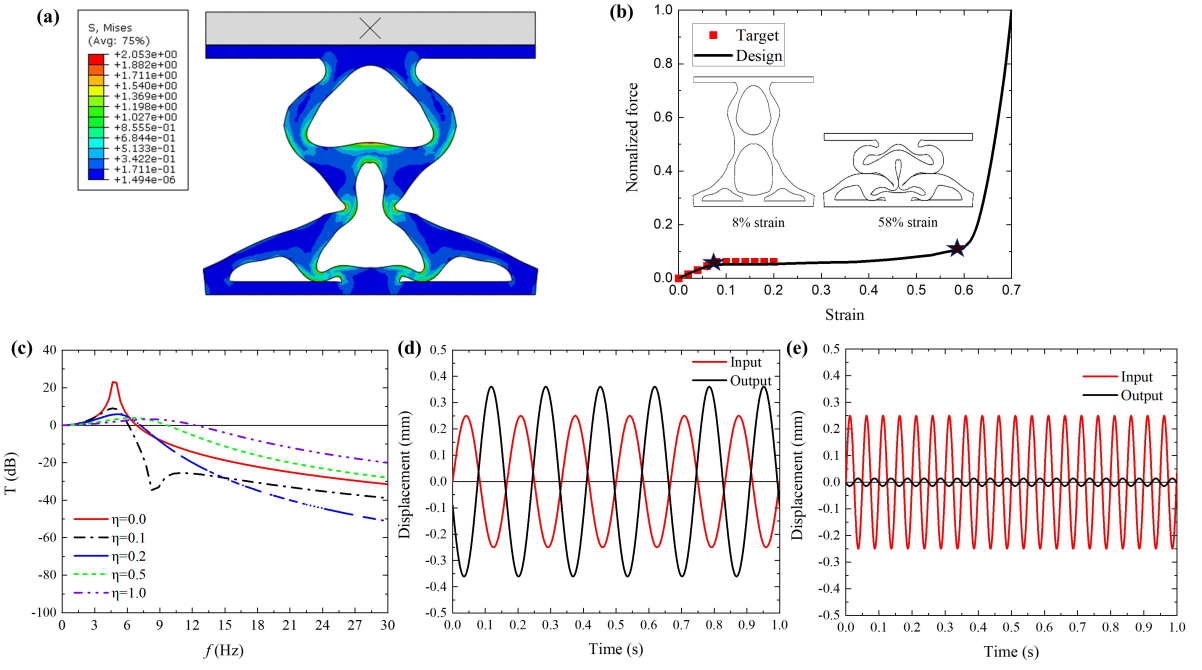

Fig. 12. Vibration isolation performance of the yield plateau structure (Design 2): (a) static deformation of the structure under a mass block; (b) force-displacement response exhibiting a yield-plateau behavior under progressive compression (force normalized by its maximum value; horizontal axis represents global engineering strain); (c) frequency-dependent transmissibility for different damping ratios; (d) comparison of periodic displacements of the base and top mass near the resonance frequency (6 Hz); (e) comparison of periodic displacements near the isolation frequency (20 Hz).

of damping, the designed isolator exhibits a resonance at 4.66 Hz and enters the isolation region (transmissibility < 1) beyond 6.66 Hz. Introducing a damping ratio of $\eta = 0.1$ significantly suppresses the resonance peak and induces an anti-resonance near 8.26 Hz. Further increases in damping lead to a smoother frequency response and a moderate upward shift of the isolation onset frequency.

To further illustrate the isolation behavior in the time domain, harmonic displacement excitations were applied at 6 Hz (near resonance) and 20 Hz (within the isolation band). As subharmonic resonance occurs under both 6 Hz and 20 Hz excitation, the harmonic components of the output displacement were extracted via Fourier transform and compared with the input displacements at those two frequencies, respectively. As shown in Fig. 12(d), excitation near resonance results in amplification, with the output displacement exceeding the input. In contrast, excitation at 20 Hz (Fig. 12(e)) leads to substantial attenuation of the transmitted motion, confirming the effectiveness of the proposed yield-plateau structure for vibration isolation. Although these two frequencies are presented as representative cases, the isolator maintains reduced transmissibility over a broad frequency range within the QZS regime. The yield-plateau response provides quasi-zero-stiffness-like behavior, which is particularly attractive for low-frequency vibration isolation.

5.3. Energy dissipation via strain softening response

This study focuses on the strain-softening (negative-stiffness) configuration of Design 3, with the loading range extended beyond the second limit point to fully activate its snap-through behavior. As illustrated in Fig. 13(a), force-controlled loading reveals abrupt transitions between two stable equilibrium branches, accompanied by distinct force jumps during both loading and unloading. This separation of equilibrium paths reflects the intrinsic hysteresis associated with limit-point instability and the corresponding energy conversion, a feature that cannot be fully captured under displacement-controlled loading of a single unit, consistent with previous observations [73].

To harness this instability-induced hysteresis for energy dissipation, multiple snap-through modules are assembled in series (Fig. 13(c)). Rigid connectors ensure effective transmission of force and displacement among adjacent units, while Rayleigh damping is introduced solely to suppress high-frequency oscillations triggered by rapid instability events. In an idealized perfectly symmetric system, all units would snap simultaneously; however, in practice,

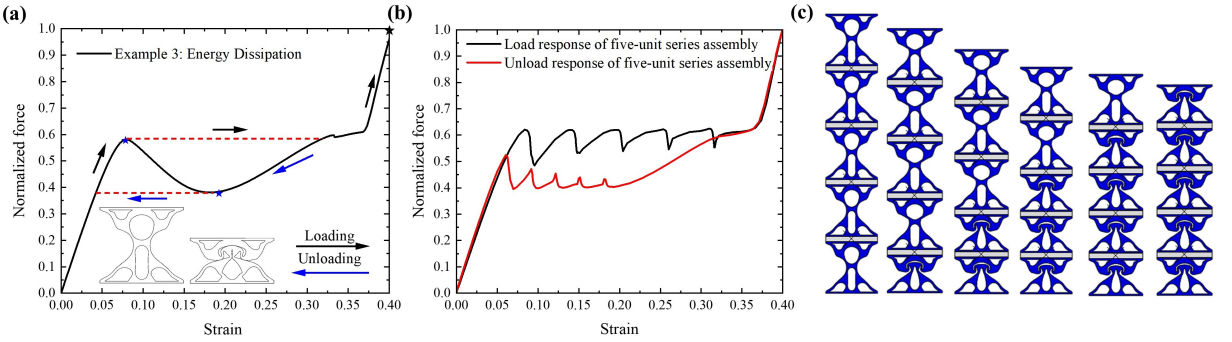

Fig. 13. Energy dissipation system based on the strain softening structure (Design 3): (a) schematic illustration of the loading-unloading process for a single unit under force control, showing snap-through events; (b) hysteresis loop of a series assembly of five units under displacement control (force normalized by its maximum value; horizontal axis represents global engineering strain); (c) configuration of the assembled architecture composed of five units.

Table 1
Reference parameter sets for the two parametric models corresponding to different target nonlinear responses.

Target Response	Parameter Set of Model 1	Parameter Set of Model 2
Strain Hardening	$(0.00, 9.78, 9.92, 3.00, -\pi/2)$	$(0.00, 5.00, 4.70, 3.00, -\pi/2)$
	$(5.00, 7.50, 1.50, 1.25, -\pi/2)$	$(5.00, 7.50, 2.20, 1.25, -\pi/2)$
	$(5.00, 3.30, 2.00, 1.20, -\pi/2)$	$(5.00, 2.50, 2.20, 1.25, -\pi/2)$
	$(2.50, 0.30, 1.85, 0.85, \pi/3)$	$(2.50, 0.30, 1.55, 0.75, \pi/3)$
Yield Plateau	$(0.00, 10.25, 9.24, 3.34, -\pi/2)$	$(0.00, 5.00, 4.70, 3.25, -\pi/2)$
	$(5.00, 7.80, 1.50, 1.18, -\pi/2)$	$(5.00, 7.50, 2.20, 1.60, -\pi/2)$
	$(5.00, 3.50, 2.00, 2.00, -\pi/2)$	$(5.00, 2.50, 2.20, 1.60, -\pi/2)$
	$(1.75, 0.30, 1.60, 0.70, \pi/3)$	$(2.50, 0.30, 1.00, 0.80, \pi/4)$
Strain Softening	$(0.00, 5.00, 4.04, 3.35, -\pi/2)$	$(0.00, 5.00, 4.04, 3.35, -\pi/2)$
	$(5.00, 7.50, 1.21, 1.50, -\pi/2)$	$(5.00, 7.50, 2.36, 1.40, -\pi/2)$
	$(5.00, 2.50, 2.36, 1.40, -\pi/2)$	$(5.00, 2.50, 1.21, 1.50, -\pi/2)$
	$(1.80, 0.30, 1.40, 0.56, \pi/3)$	$(1.80, 0.30, 1.35, 0.56, \pi/3)$

unavoidable manufacturing imperfections or deliberately introduced perturbations break this symmetry and promote sequential snap-through. In the present study, gravity is employed as a simple and controllable means to induce such imperfection.

As a result, the global force-displacement response of the assembled system (Fig. 13(b)), plotted against the global engineering strain of the assembly, exhibits a cascade of snap-through events during both loading and unloading, manifested as multiple force drops and recoveries. Here, the global engineering strain is calculated based on the cumulative deformation of the five snap-through units only, excluding the thickness of the rigid connectors. For clarity, the force is normalized by its maximum value so that the characteristic hysteretic response can be clearly visualized independent of the absolute force magnitude and the physical scale of the system. The enclosed area between the loading and unloading paths directly quantifies the mechanical energy dissipated through repeated instability-driven transitions, demonstrating the effectiveness of the strain-softening architecture as an energy-dissipation mechanism. This mechanism demonstrates how instability-induced hysteresis can be harnessed for passive energy dissipation.

5.4. Parameter models with tunnable nonlinear responses over large deformation

While topology optimization provides high design freedom, the resulting geometries are often difficult to reproduce. To address this limitation, simplified parametric models are constructed based on the dominant geometric features of the optimized designs. Based on the topology-optimized designs developed in the preceding sections, a variety of

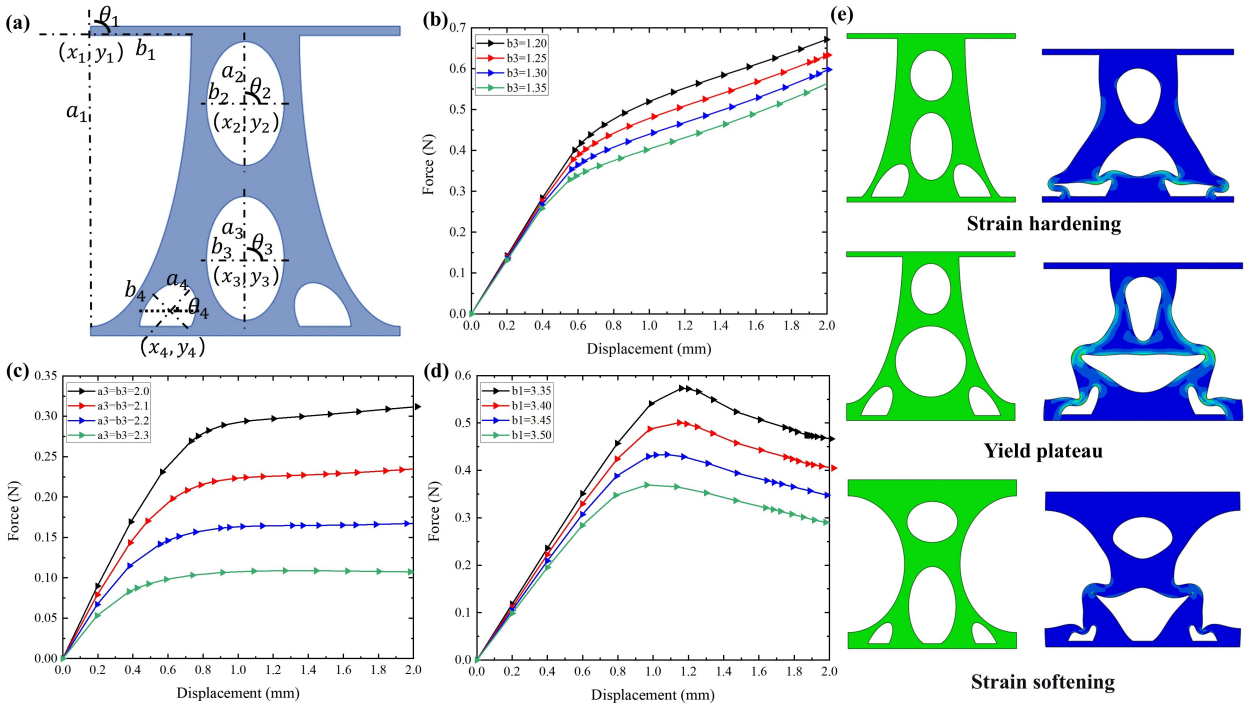

Fig. 14. Parametric model 1 based on two ellipses and its performance: (a) schematic illustration of the model with design variables; (b-d) force-displacement responses obtained by varying a small subset of geometric parameters, exhibiting strain hardening, yield plateau, and strain softening behaviors, respectively; (e) corresponding deformation patterns highlight the underlying deformation mechanisms associated with each response type.

tailored nonlinear force-displacement responses have been achieved. While these designs are directly applicable in CAE environments, they rely on complex B-spline-based geometries with a large number of control parameters, which complicates reproduction and limits their general applicability.

To improve practicality and generalizability, two simplified parametric models are constructed by abstracting the dominant geometric features of the optimized topologies. As illustrated in Fig. 14(a) of Model 1 and Fig. 15(a) of Model 2, the design variable vector $\boldsymbol{D}_m = (x_1, y_1, a_1, b_1, \theta_1, x_2, y_2, a_2, b_2, \theta_2, x_3, y_3, a_3, b_3, \theta_3, x_4, y_4, a_4, b_4, \theta_4)^\top$ defines the geometry of four ellipses, parameterized by their center coordinates (x_i, y_i), semi-major axis a_i, semi-minor axis b_i, and orientation angle θ_i. Geometric symmetry is exploited to reduce the number of independent variables: the two middle ellipses are fixed at $x_2 = x_3 = 5$ with $\theta_2 = \theta_3 = \pi/2$, one ellipse is placed at $x_1 = 0$ and mirrored accordingly, and the final ellipse is fixed at $y_4 = 0.3$, with the remaining ellipses generated symmetrically about the central axis. As a result, only 14 independent design variables are required in both models. Apart from non-intersection and topology preservation, no explicit bounds are imposed on the parameters.

Table 1 lists representative reference parameter sets for the two parametric models illustrated by Figs. 14(a) and 15(a), from which the three classes of nonlinear responses can be continuously tuned by varying only a small subset of geometric parameters.

Strain-hardening response: In Model 1, the strain-hardening behavior is primarily governed by parameter b_3. Increasing b_3 (e.g., from 1.20 to 1.35) elevates the post-buckling stiffness and the overall hardening level (Fig. 14(b)), with the dominant mechanism being stiffness reduction induced by bending of the oblique rods. In Model 2, a comparable effect is achieved by tuning parameter a_4(Fig. 15(b)), which is effective within the range [1.5, 1.75]; outside this interval, the response transitions to a strain-softening (negative-stiffness) regime.

Yield-plateau response: For Model 1, synchronously increasing $a_3 = b_3$ (from 2.0 to 2.3) progressively lowers the plateau force level while maintaining a nearly unchanged yield point (Fig. 14(c)). In Model 2, the plateau height is mainly controlled by parameters b_2 and b_3 (Fig. 15(c)), with effective tuning achieved within the range [1.4, 1.95]. The associated deformation is characterized by coordinated bending and rotation of structural components, resulting in a stable QZS-like response.

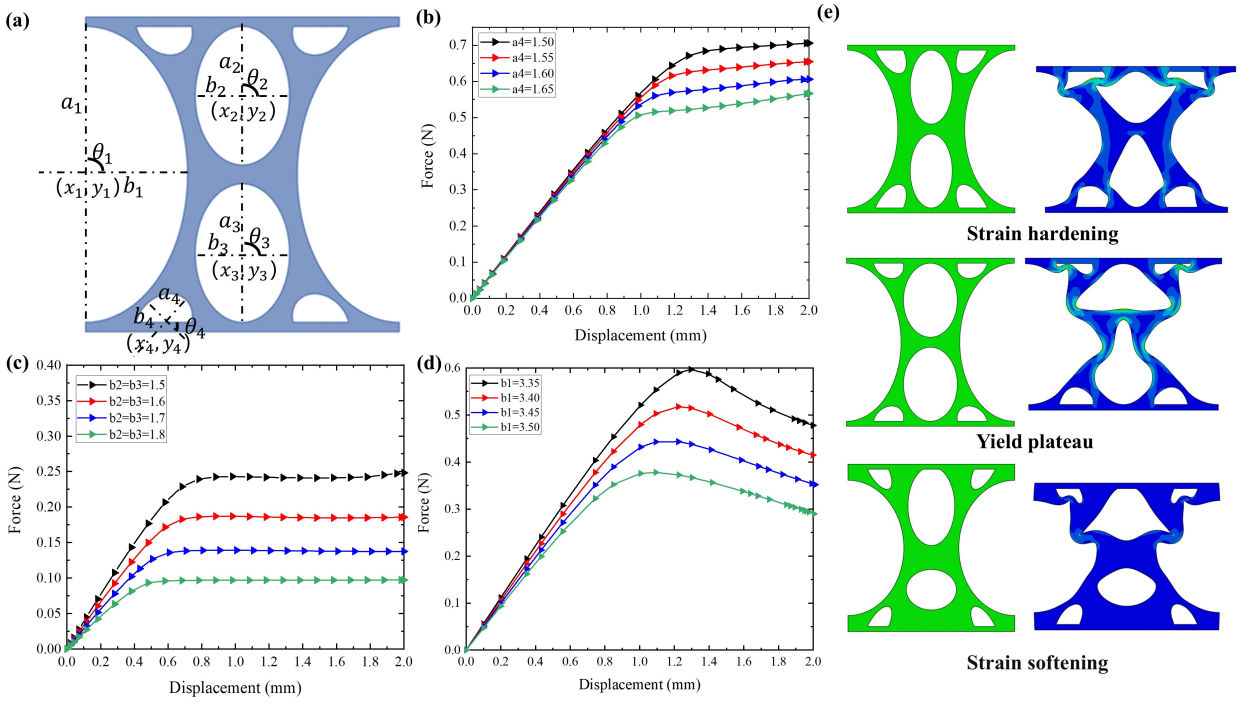

Fig. 15. Parametric model 2 based on four ellipses and its performance: (a) schematic illustration of the model with design variables; (b-d) force-displacement responses demonstrating strain hardening, yield plateau, and strain softening behaviors were achieved through parametric adjustments; (e) representative deformation patterns illustrating coordinated bending and rotation mechanisms underlying the observed nonlinear responses.

Strain-softening response: In both models (Figs. 14(d) and 15(d)), the strain-softening behavior is predominantly controlled by parameter b_1. Reducing b_1 (from 3.5 to 3.35) increases the force level (from 0.37 to 0.57) and delays the onset of the inflection point in the force-displacement curve. Owing to the simplified geometry, the deformation mechanism differs from that of the original topology-optimized designs, and pronounced snap-through behavior is no longer observed.

Overall, the proposed parametric models demonstrate that a small set of intuitive geometric parameters (such as the thickness of connecting rods (i.e., b_1, b_2, b_3) or the aspect ratio of voids (i.e., a_3, a_4)) is sufficient to reproduce a broad spectrum of nonlinear mechanical responses over large deformation. By significantly reducing geometric complexity while retaining the essential mechanical characteristics, i.e., the onset of limit-point instability and the subsequent post-buckled response, these models provide a practical bridge between topology-optimized concepts and reusable design templates. Although simplification inevitably reduces design freedom and constrains the effective parameter ranges, the parametric framework offers a transparent and extensible basis for future studies aiming at scalable design, rapid tuning, and application-oriented implementation of nonlinear mechanical metamaterials. These parametric models provide a practical bridge between topology optimization and reusable mechanical design templates.

These results motivate a broader discussion of instability-enabled response programming and its underlying mechanics.

6. Discussion: mechanics of instability-enabled response programming

The results presented above demonstrate that nonlinear mechanical responses can be systematically programmed through controlled limit-point instabilities. This section discusses the underlying mechanics, design principles, and broader implications of instability-enabled response programming.

6.1. Limit-point instability as a controllable design resource

The present results demonstrate that limit-point instability under finite deformation can be systematically exploited as a controllable design mechanism for programming nonlinear force–displacement responses. In contrast to bifurcation-induced buckling, which typically requires imperfection sensitivity analysis and often leads to strong path dependence, limit-point instability can be naturally captured under displacement-controlled loading. This feature enables the direct tracing of post-buckling equilibrium paths within the optimization loop and provides stable access to negative stiffness, force plateaus, and stiffness transitions.

More importantly, the optimized designs reveal that macroscopic nonlinear responses are not governed solely by the first occurrence of instability. Instead, they emerge from the collective behavior of multiple instability events distributed throughout the structure. The spatial location, activation sequence, and mechanical coupling of limit points determine whether the global response exhibits gradual hardening, sustained plateaus, or abrupt softening. In this sense, instability is transformed from a localized failure phenomenon into a distributed structural mechanism that can be programmed through topology optimization.

This perspective extends classical views of post-buckling mechanics by emphasizing instability-path design rather than critical-load maximization. By embedding equilibrium continuation directly into the design process, the proposed framework enables systematic exploration of nonlinear deformation landscapes that are difficult to access through conventional stability-oriented optimization. These findings establish limit-point instability as a controllable and programmable design mechanism rather than a failure mode.

6.2. Topological control of post-buckling deformation paths

Beyond instability onset, topology governs how deformation modes evolve and interact after instability. The numerical results indicate that topology plays a fundamental role in shaping post-buckling deformation paths beyond its influence on initial stiffness. In the optimized structures, topology determines not only load-carrying capacity in the pre-buckling regime, but also the redistribution of internal forces and deformation modes after instability.

For strain-hardening-type responses, primary load paths undergo a continuous transition from axial to bending-dominated deformation, weakened by auxiliary members with local instabilities. Plateau-type responses arise from a distributed instability cascade in multiple members, then maintain approximately constant force levels. In strain-softening designs, topology predisposes the structure to a local snap-through by concentrating bending and rotation in specific regions.

These observations suggest that topology optimization effectively assigns mechanical roles to different structural components, such as stabilizing elements, trigger elements, and load-redistribution pathways. The resulting nonlinear response is therefore an emergent property of interacting deformation mechanisms rather than a direct consequence of any single unstable component. This insight highlights the importance of designing topological hierarchies that regulate how instability propagates and couples across length scales.

6.3. Curvature regularization and geometric admissibility

The incorporation of a curvature constraint within the MMV framework plays a central role in ensuring the mechanical admissibility and numerical robustness of the optimized designs. Without regularization, void intersections and sharp geometric features tend to emerge during optimization, leading to artificial stress concentrations, mesh-dependent instabilities, and poor convergence behavior.

The curvature functional introduced in this work serves as a geometric regularizer rather than a physical surface energy. By penalizing excessive interface curvature reconstructed on the Eulerian grid, the method suppresses spurious corner singularities while retaining sufficient freedom for topological evolution. As demonstrated in the numerical examples, this treatment produces smooth boundaries that remain stable under large deformation and facilitate reliable sensitivity evaluation.

Importantly, the regularization does not eliminate essential instability mechanisms. Instead, it promotes mechanically meaningful geometries in which post-buckling behavior arises from distributed deformation rather than numerical artifacts. This feature is particularly important for subsequent parametric abstraction, as it ensures that the extracted templates are free from grid-scale irregularities and can be reproduced using standard CAD representations. This regularization enables robust instability programming by ensuring mechanically meaningful geometries.

6.4. Parametric abstraction and design transferability

While topology optimization provides high design freedom, the resulting geometries are often difficult to reuse in practical settings. The parametric models developed in this work demonstrate that the dominant instability mechanisms embedded in optimized topologies can be captured using a small number of intuitive geometric parameters.

The success of these models indicates that post-buckling responses are governed primarily by a limited set of geometric features, such as the relative slenderness, orientation, and spacing of key members. Once these features are identified, nonlinear responses can be efficiently retuned without repeating large-scale optimization.

This abstraction process bridges inverse design and reusable engineering templates. It suggests a hierarchical design paradigm in which topology optimization is used to discover archetypal instability mechanisms, while low-dimensional parametric models enable scalable implementation and application-specific adaptation. Such a paradigm is particularly attractive for architected materials and metamaterials, where manufacturability and design transferability are critical. This hierarchical design strategy enables scalable implementation of instability-programmed mechanical responses.

6.5. Scope, limitations, and future extensions

Several limitations of the present study should be acknowledged. First, the current framework is restricted to two-dimensional structures under quasi-static loading. Extension to three-dimensional architectures would enable richer instability modes but requires substantially increased computational effort and more sophisticated geometric control strategies.

Second, a hyperelastic constitutive model is adopted to isolate geometric nonlinearity and instability effects. While this choice facilitates mechanistic interpretation, many practical systems involve plasticity, damage, or viscoelasticity, which may interact with instability in nontrivial ways. Incorporating such material nonlinearities represents an important direction for future work.

Third, contact interactions are treated in a simplified manner and are not included in the optimization formulation. In densely deforming architectures, self-contact and friction may significantly influence post-buckling paths and energy dissipation. Integrating contact-aware sensitivity analysis into instability-based optimization remains a challenging open problem.

Finally, the present formulation focuses on prescribed quasi-static force–displacement responses. Extension to dynamic loading, impact scenarios, and stability under stochastic perturbations would further broaden the applicability of the proposed approach.

Despite these limitations, the framework establishes a general foundation for instability-enabled structural programming. By combining equilibrium path tracking, geometric regularization, and parametric abstraction, it provides a mechanics-consistent route for encoding nonlinear functionality directly into structural topology. These considerations highlight promising directions for extending instability-enabled topology optimization.

Overall, this work demonstrates that limit-point instability, when combined with topology optimization and geometric regularization, provides a systematic framework for programming nonlinear mechanical functionality. This perspective transforms instability from a constraint into a design resource and opens new opportunities for architected materials and structures.

7. Conclusion

This work demonstrates that nonlinear mechanical responses can be systematically programmed through topology optimization by exploiting limit-point instabilities under large deformation. By embedding equilibrium path tracing and curvature regularization within the Moving Morphable Void framework, an explicit design methodology is established that deliberately admits and regulates post-buckling behavior while maintaining geometric and mechanical admissibility.

The proposed framework integrates equilibrium path tracing, curvature regularization, and response-oriented optimization, enabling systematic design of instability-enabled nonlinear responses. The results reveal that macroscopic nonlinear behavior emerges from the spatial distribution and sequential activation of multiple instability modes.

Within this unified framework, structures exhibiting hardening-type, plateau-type, and softening-type responses are synthesized with high accuracy under compressive strains up to 20%. The optimized designs reveal that macroscopic nonlinear behavior is governed not merely by the onset of instability, but by the spatial distribution, sequential activation, and mechanical coupling of multiple limit-point and snap-through events embedded in the topology. These

results clarify how instability pathways, rather than isolated unstable components, serve as the fundamental carriers of programmable mechanical functionality.

The practical significance of instability-based response programming is demonstrated through representative applications in overload protection, low-frequency vibration isolation, and instability-driven energy absorption. By exploiting geometric nonlinearity instead of irreversible material damage, the proposed architectures enable reversible, tunable, and mechanically robust performance over large deformation ranges.

To enhance design transferability, low-dimensional parametric templates are extracted from representative optimized topologies. These templates preserve the essential instability mechanisms while enabling efficient retuning using a small number of intuitive geometric parameters, thereby bridging high-fidelity topology optimization and reusable engineering design.

More broadly, this study advances topology optimization from stiffness- and stability-oriented design toward instability-path engineering, in which equilibrium trajectories under large deformation are explicitly shaped to encode target force–displacement responses. The proposed framework provides a mechanics-consistent foundation for developing reusable, hierarchical, and multifunctional architected materials whose nonlinear behavior is programmed directly through controlled limit-point instability. Extensions to three-dimensional architectures, inelastic materials, and dynamic loading conditions represent promising directions for future research. This framework provides a new paradigm for designing architected materials with programmable mechanical functionality.

A. Sensitivity derivation of the MMV-TDF with respect to design variables

In the two-dimensional MMV method explicitly described by B-spline curves, the analytical sensitivity of the topological description function ϕ_i^{v} for the i-th hole with respect to its s-th design variable d_i^s is derived as follows:

$$\begin{aligned}
&\frac{\partial \phi_i^{\mathrm{v}}(\boldsymbol{D}_i;\boldsymbol{x})}{\partial x_{0i}} = \frac{x_{0i}-x}{\sqrt{(x-x_{0i})^2+(y-y_{0i})^2}}, \quad \frac{\partial \phi_i^{\mathrm{v}}(\boldsymbol{D}_i;\boldsymbol{x})}{\partial y_{0i}} = \frac{y_{0i}-y}{\sqrt{(x-x_{0i})^2+(y-y_{0i})^2}}, \\
&\frac{\partial \phi_i^{\mathrm{v}}(\boldsymbol{D}_i;\boldsymbol{x})}{\partial d_{j,i}} = \frac{1}{r_i(\theta)}\left(C_{i,x}(\theta)\frac{\partial C_{i,x}}{\partial d_{j,i}} + C_{i,y}(\theta)\frac{\partial C_{i,y}}{\partial d_{j,i}}\right),
\end{aligned} \tag{A.1}$$

where $d_{j,i}$ represents the distance from the j-th control point of the i-th hole to its center, with $1 \le j \le n$, and n is the total number of control points. Additionally, we have:

$$\frac{\partial C_{i,x}}{\partial d_{j,i}} = \sum_{k=0}^{n+1} N_{k,p}(\mu(\theta))\frac{\partial P_{k,i}^x}{\partial d_{j,i}}, \quad \frac{\partial C_{i,y}}{\partial d_{j,i}} = \sum_{k=0}^{n+1} N_{k,p}(\mu(\theta))\frac{\partial P_{k,i}^y}{\partial d_{j,i}}, \tag{A.2}$$

where $P_{k,i}^x$ and $P_{k,i}^y$ denote the coordinates of the k-th control point of the i-th hole in the x- and y-directions, respectively. If $k = j$, $\frac{\partial P_{k,i}^x}{\partial d_{j,i}}$ and $\frac{\partial P_{k,i}^y}{\partial d_{j,i}}$ can be computed as:

$$\frac{\partial P_{k,i}^x}{\partial d_{j,i}} = \cos(\theta_j), \quad \frac{\partial P_{k,i}^y}{\partial d_{j,i}} = \sin(\theta_j), \tag{A.3}$$

otherwise, $\frac{\partial P_{k,i}^x}{\partial d_{j,i}} = 0$ and $\frac{\partial P_{k,i}^y}{\partial d_{j,i}} = 0$.

B. Optimal design minimizing end compliance (stiffness maximization)

To further evaluate the proposed maximum energy design, a general design methodology incorporating both geometric and material nonlinearities is presented here. The objective function is to minimize the end compliance, or specifically, the negative value of the product of the reaction force and the terminal displacement. In Eq. (17), the objective function only needs to be modified as:

$$\mathcal{J}_3(\boldsymbol{U}_{\mathrm{fn}}(\boldsymbol{D}),\boldsymbol{D}) = -\overline{\boldsymbol{U}}_{\mathrm{dn}}^{\top}\boldsymbol{F}_{\mathrm{dn}}(\boldsymbol{U}_{\mathrm{fn}},\boldsymbol{D}), \tag{B.4}$$

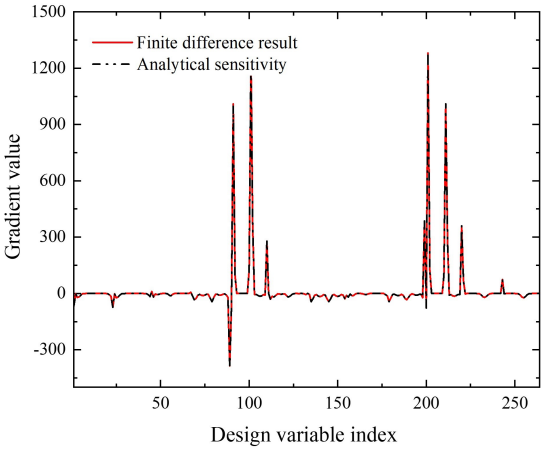

Fig. S1. Differential sensitivity verification for tailored nonlinear force–displacement responses design.

where $\overline{\boldsymbol{U}}_{\mathrm{dn}}$ corresponds to the applied displacement field and the other variables are defined consistently with the main text. The Lagrangian augmentation function is defined by introducing the adjoint displacement vectors $\boldsymbol{\lambda}$:

$$L_3(\boldsymbol{U}, \boldsymbol{D}) = \mathcal{J}_3(\boldsymbol{U}_{\mathrm{fn}}(\boldsymbol{D}), \boldsymbol{D}) + \boldsymbol{\lambda}^{\top} \boldsymbol{R}(\boldsymbol{U}, \boldsymbol{D}), \tag{B.5}$$

where $\boldsymbol{R}$ denotes the residual vector. The derivative of the Lagrangian with respect to the design variables is then given by

$$\frac{\partial L_3(\boldsymbol{U}, \boldsymbol{D})}{\partial \boldsymbol{D}} = \boldsymbol{\lambda}_{\mathrm{dn}}^{\top} \frac{\partial \boldsymbol{f}_{\mathrm{dn}}^{\mathrm{int}}}{\partial \boldsymbol{D}} + \boldsymbol{\lambda}_{\mathrm{fn}}^{\top} \frac{\partial \boldsymbol{f}_{\mathrm{fn}}^{\mathrm{int}}}{\partial \boldsymbol{D}}. \tag{B.6}$$

By applying the adjoint method, the adjoint vectors are chosen as

$$\boldsymbol{\lambda}_{\mathrm{dn}} = -\overline{\boldsymbol{U}}_{\mathrm{dn}}, \qquad \boldsymbol{\lambda}_{\mathrm{fn}}^{\top} = \overline{\boldsymbol{U}}_{\mathrm{dn}}^{\top} \frac{\partial \boldsymbol{f}_{\mathrm{dn}}^{\mathrm{int}}}{\partial \boldsymbol{U}_{\mathrm{fn}}} \left(\frac{\partial \boldsymbol{f}_{\mathrm{fn}}^{\mathrm{int}}}{\partial \boldsymbol{U}_{\mathrm{fn}}} \right)^{-1}. \tag{B.7}$$

With those results in mind, the optimal design maximizing structural stiffness can be obtained.

C. Finite difference verification for Problem I

Finite-difference verification was performed to assess the consistency of the adjoint sensitivities for Problem I using the boundary conditions and initial design illustrated in Fig. 6(a). Analytical sensitivities were compared against finite-difference approximations for representative design variables.

As shown in Fig. S1, excellent agreement is observed between analytical and finite-difference results, confirming the correctness of the sensitivity implementation. Sensitivity magnitudes differ between the response-based and energy-based objectives ($\mathcal{O}(10^3)$ vs. $\mathcal{O}(10^{-1})$), reflecting the stronger nonlinearity of the response-based formulation, but the close match validates the gradient computations for both formulations.

D. Additional design examples and extended analyses

This appendix presents additional optimized designs exhibiting nonlinear mechanical responses, obtained using the topology optimization framework and shown in Fig. S2.

Extended analysis of strain hardening designs. Two additional strain-hardening structures are examined to illustrate alternative stiffness transitions and topological realizations within the same response class.

- **Design 4** targets a stiffness reduction from 0.25 N/mm to 0.1 N/mm, with a relative error of 0.8%. Compared with the corresponding design in the main text, the central load-bearing region is more compact, leading to a more

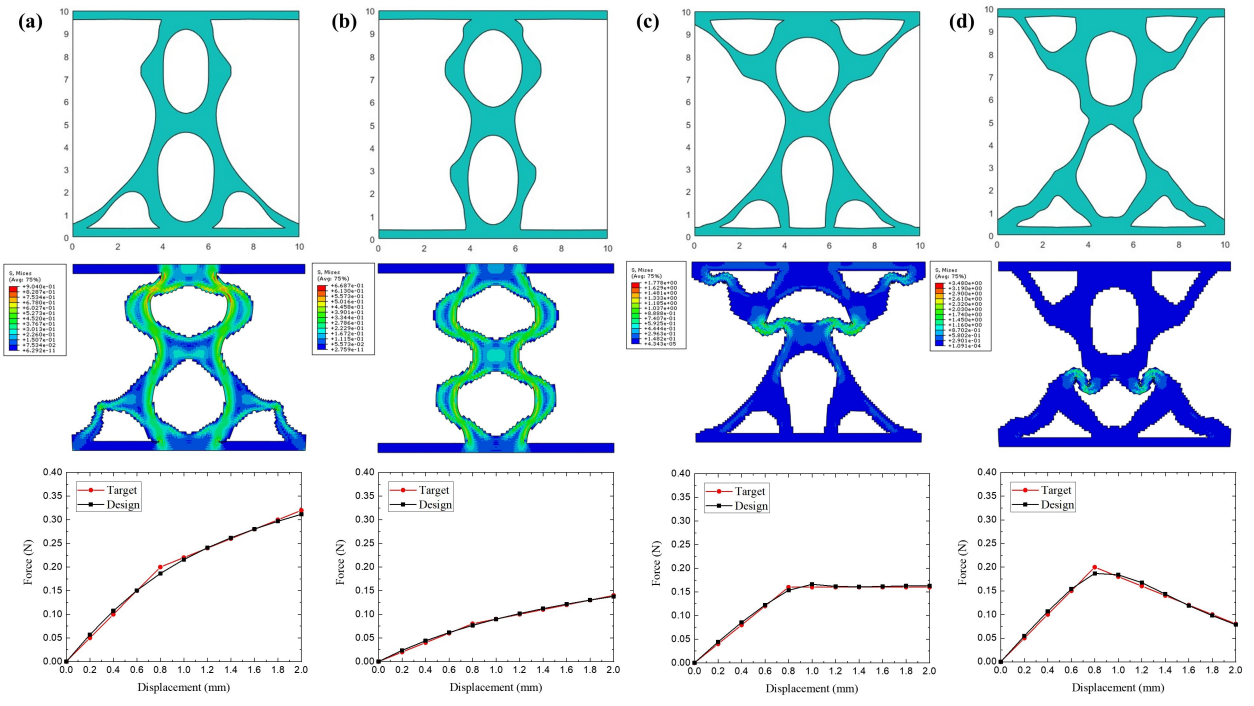

Fig. S2. Additional design examples obtained using the proposed framework: (a) Design 4 (strain hardening response); (b) Design 5 (strain hardening response); (c) Design 6 (yield plateau response); (d) Design 7 (strain softening response). Each case shows the optimized topology, stress distribution at a representative deformation state under background grid, and the achieved force–displacement response.

uniform material distribution. The two oblique members exhibit non-uniform cross-sections, being thicker near their bases and more slender toward the top. Under increasing displacement, the slender segments undergo small local limit-point instabilities that modulate the effective stiffness, while the compact central region maintains the primary load-bearing function, resulting in a smooth post-transition response.

- **Design 5** targets a transition from 0.1 N/mm to 0.05 N/mm, with a relative error of 0.7%. This design adopts an "8"-shaped structure with strategically thickened regions within the main frame. During the initial loading stage, the reinforced segments provide efficient load transfer, while weaker segments experience minor local instabilities that contribute to gradual stiffness reduction without altering the global deformation mode.

These examples demonstrate that strain-hardening responses are primarily governed by bending deformation within the main load-bearing framework, while auxiliary members or locally reinforced segments serve a secondary role by modulating stiffness through controlled local instabilities.

Extended analysis of yield plateau designs. **Design 6** provides an additional yield-plateau example with an initial stiffness of 0.2 N/mm (relative error of 1.7%). The optimized topology consists of slender, rod-like members. Despite the topological differences from the cases presented in the main text, the resulting force-displacement response confirms that the plateau behavior arises from the sequential activation of instabilities in multiple members, rather than from a single dominant instability event.

Extended analysis of strain softening designs. **Design 7** targets an initial stiffness of 0.25 N/mm and a more pronounced negative post-instability slope of −0.1 N/mm, with a relative error of 2%. The post-buckling load drop is realized through a concentrated global limit-point instability accompanied by branch switching. While the detailed local stress distribution varies, the overall deformation pattern follows the same mechanism as the main-text strain-softening design, demonstrating that topology can localize instability to produce negative stiffness while preserving residual load-bearing capacity.

CRediT authorship contribution statement

Zongliang Du: Conceptualization, Supervision, Investigation, Writing - original draft, Writing - review & editing. **Tanghuai Bian:** Methodology, Investigation, Formal analysis, Validation, Software, Writing-original draft. **Yunhang Guo:** Methodology, Investigation, Formal analysis. **Zhiang Xu:** Methodology, Investigation, Formal analysis. **Anxian Huang:** Methodology, Investigation, Formal analysis. **Huajian Gao:** Supervision, Writing - review & editing. **Xu Guo:** Supervision, Writing - review & editing.

Declaration of competing interest

The authors declare that they have no known competing financial interests or personal relationships that could have appeared to influence the work reported in this paper.

Acknowledgment

We acknowledge the help of Professor Rui Zhu from the Beijing Institute of Technology and Professor Xiaopeng Zhang from the Dalian University of Technology in the simulation of Section 5.

References

[1] Pengcheng Jiao, Jochen Mueller, Jordan R. Raney, Xiaoyu Zheng, and Amir H. Alavi. Mechanical metamaterials and beyond. *Nature Communications*, 14:6004, 2023.

[2] Pingqiang Cai, Changxian Wang, Huajian Gao, and Xiaodong Chen. Mechanomaterials: a rational deployment of forces and geometries in programming functional materials. *Advanced Materials*, 33(46):2007977, 2021.

[3] Qiguang He, Samuele Ferracin, and Jordan R. Raney. Programmable responsive metamaterials for mechanical computing and robotics. *Nature Computational Science*, 4:567–573, 2024.

[4] Sinha Prakhar and Mukhopadhyay Tanmoy. Programmable multi-physical mechanics of mechanical metamaterials. *Materials Science and Engineering: R: Reports*, 155:100745, 2023.

[5] Chenyang Liu, Xi Zhang, Jiahui Chang, You Lyu, Jianan Zhao, and Song Qiu. Programmable mechanical metamaterials: basic concepts, types, construction strategies—a review. *Frontiers in Materials*, 11:1–33, 2024.

[6] Sheng Xu, Zheng Yan, Kyung-In Jang, Wen Huang, Haoran Fu, Jeonghyun Kim, Zijun Wei, Matthew Flavin, Joselle McCracken, Renhan Wang, et al. Assembly of micro/nanomaterials into complex, three-dimensional architectures by compressive buckling. *Science*, 347(6218): 154–159, 2015.

[7] Katia Bertoldi, Vincenzo Vitelli, Johan Christensen, and Martin van Hecke. Flexible mechanical metamaterials. *Nature Reviews Materials*, 2:17066, 2017.

[8] Raouf A. Ibrahim. Recent advances in nonlinear passive vibration isolators. *Journal of Sound and Vibration*, 314(3):371–452, 2008.

[9] Yuqi Xu, Haowen Dong, and Yuesheng Wang. Topology optimization of programable quasi-zero-stiffness metastructures for low-frequency vibration isolation. *International Journal of Mechanical Sciences*, 280:109557, 2024.

[10] Wenlong Liu, Quan Zhang, Lingling Wu, Jingbo Sun, and Ji Zhou. Design of quasi-zero stiffness metamaterials with high reliability via metallic architected materials. *Thin-Walled Structures*, 198:111686, 2024.

[11] Chao Ma, Kun Wu, Yanfeng Wang, and Yuesheng Wang. Customized design of periodic metacushion with quasi-zero-stiffness for low-frequency vibration isolation. *International Journal of Solids and Structures*, 320:113518, 2025.

[12] Yue Hu, Jianlei Zhao, Hao Zhou, Ivana Kovacic, Runan Hua, Honggang Li, and Rui Zhu. Integrated design of thermally actuated metastructure for modulatable dual vibration isolation function. *Engineering Structures*, 353:122271, 2026.

[13] Hiromi Yasuda, Yasuhiro Miyazawa, Efstathios G. Charalampidis, Christopher Chong, Panayotis G. Kevrekidis, and Jinkyu Yang. Origami-based impact mitigation via rarefaction solitary wave creation. *Science Advances*, 5(5):eaau2835, 2019.

[14] Lawrence Smith, Brandon Hayes, Kurtis Ford, Elizabeth Smith, David Flores, and Robert MacCurdy. Tunable metamaterials for impact mitigation. *Advanced Materials Technologies*, 9(6):2301668, 2024.

[15] Aaron McCrary, Mohammad Saber Hashemi, and Azadeh Sheidaei. Programmable bidirectional mechanical metamaterial with tunable stiffness and frictional energy dissipation. *Advanced Theory and Simulations*, 5(7):2200135, 2022.

[16] William Isaac Chukwuemeke and Duddeck Fabian. Recent progress in 4d printed energy-absorbing metamaterials and structures. *Virtual and Physical Prototyping*, 18(1):e2197436, 2023.

[17] Zhiqiang Meng, Mingchao Liu, Yafei Zhang, and Changqing Chen. Multi-step deformation mechanical metamaterials. *Journal of the Mechanics and Physics of Solids*, 144:104095, 2020.

[18] Kuan Liang, Yaguang Wang, Yangjun Luo, Akihiro Takezawa, Xiaopeng Zhang, and Zhan Kang. Programmable and multistable metamaterials made of precisely tailored bistable cells. *Materials & Design*, 227:111810, 2023.

[19] Eric Carnoy and Guy Sander. Stability and postbuckling analysis of nonlinear structures. *Computer Methods in Applied Mechanics and Engineering*, 32(1):329–363, 1982.

[20] Alphose Zingoni, Mark Bradford, and Leroy Gardner. Advances in buckling: Mechanics, analysis and design. *Structures*, 69:107535, 2024.

[21] Samir Emam and Walter Lacarbonara. A review on buckling and postbuckling of thin elastic beams. *European Journal of Mechanics - A/Solids*, 92:104449, 2022.

[22] Zhichao Fan, Keh-Chih Hwang, John A Rogers, Yonggang Huang, and Yihui Zhang. A double perturbation method of postbuckling analysis in 2d curved beams for assembly of 3d ribbon-shaped structures. *Journal of the Mechanics and Physics of Solids*, 111:215–238, 2018.

[23] Claudio Findeisen, Jörg Hohe, Muamer Kadic, and Peter Gumbsch. Characteristics of mechanical metamaterials based on buckling elements. *Journal of the Mechanics and Physics of Solids*, 102:151–164, 2017.

[24] Johannes T.B. Overvelde, Tamara Kloek, Jonas J. A. D'haen, and Katia Bertoldi. Amplifying the response of soft actuators by harnessing snap-through instabilities. *Proceedings of the National Academy of Sciences of the United States of America*, 112(35):10863–10868, 2015.

[25] Hao Deng, Lin Cheng, Xuan Liang, Devlin Hayduke, and Alber C. To. Topology optimization for energy dissipation design of lattice structures through snap-through behavior. *Computer Methods in Applied Mechanics and Engineering*, 358:112641, 2020.

[26] Zhongwen Zhang, Liwei Chen, and Zhaodong Xu. Snap-through behavior of bistable beam with variable sections: mechanical model and experimental study. *Smart Materials and Structures*, 31(10):105004, 2022.

[27] Yingchao Peng, Imtiar Niloy, Megan Kam, Paolo Celli, and Paul Plucinsky. Programming bistability in geometrically perturbed mechanical metamaterials. *Physical Review Applied*, 22:014073, 2024.

[28] Jin Qiu, Jeffrey H. Lang, and Alexander H. Slocum. A curved-beam bistable mechanism. *Journal of Microelectromechanical Systems*, 13(2): 137–146, 2004.

[29] Huang Zhang, Jun Wu, Yihui Zhang, and Daining Fang. Multistable mechanical metamaterials: A brief review. *Transactions of Nanjing University of Aeronautics & Astronautics*, 38(1):1, 2021.

[30] Jiajia Shen, Martin Garrad, Qicheng Zhang, Olivia Leao, Alberto Pirrera, and Rainer M. J. Groh. Active reconfiguration of multistable metamaterials for linear locomotion. *Physical Review B*, 107:214103, 2023.

[31] Chengjun Zeng, Liwu Liu, Yunqiang Hu, Wei Zhao, Xiaozhou Xin, Yanju Liu, and Jinsong Leng. Stair-stepping mechanical metamaterials with programmable load plateaus. *Advanced Functional Materials*, 34(49):2408887, 2024.

[32] Yuling Wei, Fei Pan, Xin Lin, Lei Zhang, Jinwu Xiang, and Yuli Chen. On-demand reprogrammable mechanical metamaterial driven by structure-performance relations. *Advanced Materials*, 37(9):2410865, 2024.

[33] Xin Lin, Fei Pan, Yong Ma, Yuling Wei, Kang Yang, Zihong Wu, Juan Guan, Bin Ding, Bin Liu, Jinwu Xiang, and Yuli Chen. Mechanical Fourier transform for programmable metamaterials. *Proceedings of the National Academy of Sciences*, 120(37):e2305380120, 2023.

[34] Shahram Janbaz, FSL Bobbert, Mohammad J Mirzaali, and Amir A Zadpoor. Ultra-programmable buckling-driven soft cellular mechanisms. *Materials Horizons*, 6(6):1138–1147, 2019.

[35] Ahmad Rafsanjani, Abdolhamid Akbarzadeh, and Damiano Pasini. Snapping mechanical metamaterials under tension. *Advanced Materials*, 27(39):5931–5935, 2015.

[36] Jian He, Tianbao Liang, Yaohui Wang, Liang Xia, and Yi Xiong. Quasi-zero stiffness metamaterials with programmable multistability for multi-scenario applications. *Applied Materials Today*, 46:102864, 2025.

[37] Aniket Pal and Metin Sitti. Programmable mechanical devices through magnetically tunable bistable elements. *Proceedings of the National Academy of Sciences of the United States of America*, 120(15):e2212489120, 2023.

[38] Jian Hua, Yuan Zhou, Zhiqiang Meng, and Changqing Chen. Pre-compressed beam-based multistable mechanical metamaterials with programmable loading and unloading deformation sequences. *Thin-Walled Structures*, 209:112879, 2025.

[39] Ole Sigmund and Kurt Maute. Topology optimization approaches. *Structural and Multidisciplinary Optimization*, 48(6):1031–1055, 2013.

[40] Guilin Wen, Jie Liu, Zijie Chen, Peng Wei, Kai Long, Hongxin Wang, Jianhua Rong, and Yimin Xie. A survey of nonlinear continuum topology optimization methods. *Chinese Journal of Theoretical and Applied Mechanics*, 54(10):2659–2675, 2022.

[41] Weichen Li, Fengwen Wang, Ole Sigmund, and Xiaojia Shelly Zhang. Design of composite structures with programmable elastic responses under finite deformations. *Journal of the Mechanics and Physics of Solids*, 151:104356, 2021.

[42] Yifu Lu, Quantian Luo, and Liyong Tong. Topology optimization for metastructures with quasi-zero stiffness and snap-through features. *Computer Methods in Applied Mechanics and Engineering*, 434:117587, 2025.

[43] Fengwen Wang, Ole Sigmund, and Jakob Søndergaard Jensen. Design of materials with prescribed nonlinear properties. *Journal of the Mechanics and Physics of Solids*, 69(49):156–174, 2014.

[44] Dilaksan Thillaithevan, Ryan Murphy, Robert Hewson, and Matthew Santer. Inverse design of periodic microstructures with targeted nonlinear mechanical behaviour. *Structural and Multidisciplinary Optimization*, 67:55–71, 2024.

[45] Jiashuo Xu, Mi Xiao, and Liang Gao. Inverse design of structures with accurately programmable nonlinear mechanical responses by topology optimization. *Computer Methods in Applied Mechanics and Engineering*, 446:118243, 2025.

[46] Qi Cai, Ruoqiang Feng, and Zhijie Zhang. Topology optimization of trusses incorporating practical local buckling stability considerations. *Structures*, 41:1710–1718, 2022.

[47] Anna Dalklint, Mathias Wallin, and Daniel A. Tortorelli. Structural stability and artificial buckling modes in topology optimization. *Structural and Multidisciplinary Optimization*, 64:1751–1763, 2021.

[48] Bing Yi, Yuqing Zhou, Gil Ho Yoon, and Kazuhiro Saitou. Topology optimization of functionally-graded lattice structures with buckling constraints. *Computer Methods in Applied Mechanics and Engineering*, 354:593–619, 2019.

[49] Tao Xu, Huang Xiaodong, Xiaoshan Lin, and Yimin Xie. Topology optimization for maximizing buckling strength using a linear material model. *Computer Methods in Applied Mechanics and Engineering*, 417:116437, 2023.

[50] Jianjun Wang, Jianping Han, and Jixiang Xu. Hysteretic behavior of resilient rocking column bases: Experimental validation and numerical investigation. *Journal of Building Engineering*, 115:114588, 2025.

[51] Ghandil Mehdi, Tajmir Riahi Hossein, and Behnamfar Farhad. Numerical and experimental studies of a new visco-plastic drawing damper for control of structures under high and low-amplitude excitations. *Soil Dynamics and Earthquake Engineering*, 201:109918, 2026.

[52] Shiwei Liu, Gaoliang Peng, Zhixiong Li, Weihua Li, and Lidong Sun. Low-frequency vibration isolation via an elastic origami-inspired structure. *International Journal of Mechanical Sciences*, 260:108622, 2023.

[53] Lei Xiao, Xiang Sun, Li Cheng, and Xiang Yu. A 3d-printed quasi-zero-stiffness isolator for low-frequency vibration isolation: Modelling and experiments. *Journal of Sound and Vibration*, 577:118308, 2024.

[54] Hongye Ma, Ke Wang, Haifeng Zhao, Wubin Shi, Jing Xue, Yanlin Zhou, Qiushi Li, Gong Wang, and Bo Yan. Energy dissipation and shock isolation using novel metamaterials. *International Journal of Mechanical Sciences*, 228:107464, 2022.

[55] Zhi Zhao, Rahul Dev Kundu, Ole Sigmund, and Xiaojia Shelly Zhang. Extreme nonlinearity by layered materials through inverse design. *Science Advances*, 11(20):eadr6925, 2025.

[56] Scott Townsend and H. Alicia Kim. A level set topology optimization method for the buckling of shell structures. *Structural and Multidisciplinary Optimization*, 60(5):1783–1800, 2019.

[57] Angelo Luongo, Manuel Ferretti, and Simona Di Nino. *Stability and Bifurcation of Structures: Statical and Dynamical Systems*. Springer, Cham, Switzerland, 1st edition, 2023.

[58] Jiaming Guo and Changguo Wang. Path tracking of buckling instability in flexible structures. *International Journal of Mechanical Sciences*, 310:111073, 2026.

[59] Ellen M. Arruda and Mary C. Boyce. A three-dimensional constitutive model for the large stretch behavior of rubber elastic materials. *Journal of the Mechanics and Physics of Solids*, 41(2):389–412, 1993.

[60] Klaus-Jürgen Bathe. *Finite Element Procedures*. Klaus-Jürgen Bathe, Watertown, MA, USA, 2nd edition, 2006.

[61] Mike A. Crisfield. *Non-linear Finite Element Analysis of Solids and Structures, Volume 1: Essentials*. John Wiley & Sons, Chichester, 1991.

[62] Ted Belytschko, Wing Kam Liu, Brian Moran, and Khalil Elkhodary. *Nonlinear Finite Elements for Continua and Structures*. Wiley, Chichester, England, 2nd edition, 2014.

[63] Zongliang Du, Tianchen Cui, Chang Liu, Weisheng Zhang, Yilin Guo, and Xu Guo. An efficient and easy-to-extend matlab code of the moving morphable component (mmc) method for three-dimensional topology optimization. *Structural and Multidisciplinary Optimization*, 65(5):158, 2022.

[64] Yunhang Guo, Zongliang Du, Chang Liu, Weisheng Zhang, Riye Xue, Yilin Guo, Shan Tang, and Xu Guo. Explicit topology optimization of three-dimensional geometrically nonlinear structures. *Acta Mechanica Sinica*, 39:423084, 2023.

[65] Krister Svanberg. The method of moving asymptotes—a new method for structural optimization. *International Journal for Numerical Methods in Engineering*, 24(2):359–373, 1987.

[66] Xiaodong Huang and Mike Xie. Topology optimization of nonlinear structures under displacement loading. *Engineering Structures*, 30(7): 2057–2068, 2008.

[67] Ivana Kovacic, Michael J. Brennan, and Timothy P. Waters. A study of a nonlinear vibration isolator with a quasi-zero stiffness characteristic. *Journal of Sound and Vibration*, 315(3):700–711, 2008.

[68] Feng Zhao, Jinchen Ji, Shuqian Cao, Jingyang Zheng, and Quantian Luo. A constant quasi-zero stiffness isolator with tension springs to isolate vibrations with ultralow frequency. *International Journal of Non-Linear Mechanics*, 175:105129, 2025.

[69] Hong-Tai Zhang, Rui Zhang, and Zhenduo Yan. Experimental and numerical evaluation of rocking column bases with friction connections and vertical web plates. *Journal of Building Engineering*, 114:114449, 2025.

[70] Chaoran Liu, Wei Zhang, Kaiping Yu, Tao Liu, and Yan Zheng. Quasi-zero-stiffness vibration isolation: Designs, improvements and applications. *Engineering Structures*, 301:117282, 2024.

[71] Yonglei Zhang, Hao Wen, Haiyan Hu, and Dongping Jin. A novel quasi-zero stiffness isolator with designable stiffness using cam-roller-spring-rod mechanism. *Acta Mechanica Sinica*, 41:524210, 2024.

[72] Stephen P. Timoshenko, Donovan Harold Young, and William Jr. Weaver. *Vibration Problems in Engineering*. John Wiley & Sons, New York, USA, 4th edition, 1974.

[73] David Restrepo, Nilesh D. Mankame, and Pablo D. Zavattieri. Phase transforming cellular materials. *Extreme Mechanics Letters*, 4:52–60, 2015.